Mon. Not. R. Astron. Soc. **000**, 1–?? (2014) Printed 13 October 2014 (MN LATEX style file v2.2)

Ambient magnetic field amplification in shock fronts of relativistic jets: an application to GRB afterglows

G. Rocha da Silva[1]; D. Falceta-Gonçalves[2,3⋆]; G. Kowal[3]; E. M. de Gouveia Dal Pino[1]
[1] *Instituto de Astronomia, Geofísica e Ciências Atmosféricas, Universidade de São Paulo, Rua do Matão 1226, CEP: 05508-090, São Paulo, Brazil*
[2] *SUPA, School of Physics & Astronomy, University of St Andrews, North Haugh, St Andrews, Fife KY16 9SS, UK*
[3] *Escola de Artes, Ciências e Humanidades, Universidade de São Paulo, Rua Arlindo Bettio 1000, CEP 03828-000, São Paulo, Brazil*

arXiv:1410.2776v1 [astro-ph.HE] 10 Oct 2014

ABSTRACT

Strong downstream magnetic fields of order of $\sim$ 1G, with large correlation lengths, are believed to cause the large synchrotron emission at the afterglow phase of gamma ray bursts (GRBs). Despite of the recent theoretical efforts, models have failed to fully explain the amplification of the magnetic field, particularly in a matter dominated scenario. We revisit the problem by considering the synchrotron emission to occur at the expanding shock front of a weakly magnetized relativistic jet over a magnetized surrounding medium. Analytical estimates and a number of high resolution 2D relativistic magneto-hydrodynamical (RMHD) simulations are provided. Jet opening angles of $\theta = 0^\circ - 20^\circ$, and ambient to jet density ratios of $10^{-4} - 10^2$ were considered. We found that most of the amplification is due to compression of the ambient magnetic field at the contact discontinuity between the reverse and forward shocks at the jet head, with substantial pile-up of the magnetic field lines as the jet propagates sweeping the ambient field lines. The pile-up is maximum for $\theta \to 0$, decreasing with θ, but larger than in the spherical blast problem. Values obtained for certain models are able to explain the observed intensities. The maximum correlation lengths found for such strong fields is of $l_{\rm corr} \leqslant 10^{14}$cm, $2-6$ orders of magnitude larger than the found in previous works.

Key words: shock waves - ISM: magnetic fields, supernovae, jets and outflows - (stars:) gamma-ray burst: general - methods: numerical

1 INTRODUCTION

Gamma ray bursts (GRBs) liberate a significant fraction of the rest-mass energy of their source ($> 10^{51}$ erg) over intervals ranging from a fraction of a second to minutes. The standard fireball picture (Paczyński 1986; Shemi & Piran 1990; Rees & Meszaros 1992; Sari et al. 1996) explains the otherwise puzzling ability of such sources to vary on short timescales by arguing that the bursts are produced via a relativistic outflow with a bulk Lorentz factor $\Gamma > 100$. At first, the relativistic flow is dissipated internally (via internal shocks or via another form of internal dissipation, like magnetic instabilities) that produce the prompt γ-rays. Later the interaction of the flow with the circum-burst matter produces an external shock and this blast wave produces the subsequent afterglow at lower frequencies. Observational clues concerning GRB progenitors indicate that supernova explosions of massive stars could be the predominant sources of long GRBs (i.e. those whose gamma emission lasts more than 2 secs and the standard model for these objects is the Collapsar model (Woosley 1993; Paczyński 1998; MacFadyen & Woosley 1999). The main possible sources of short GRBs are mergers of neutron stars (NSs) with other NSs, or with black holes (Eichler & Cheng 1989), although other driving sources such as phase transition of a NS to a quark star have also been proposed (Lugones et al. 2002).

The field of GRBs has rapidly advanced in recent years, especially following the launches of NASA missions *Swift* and *Fermi*, both in the past decade. Due to their elusive nature, observing GRBs in all wavelengths at all epochs (including during and after the GRB) is still challenging with the current GRB detectors and follow up telescopes. As a result, for every new temporal or spectral window unveiled a rich trove of new phenomenology is uncovered (Zhang 2011). The new observations have raised new questions.

The composition of the relativistic jets that arise in GRBs is uncertain due to the lack of direct observations. The most important unknown parameter is the ratio (σ) between the Poynting flux and the matter flux (here both baryons and leptons are considered). In the standard fireball

⋆ E-mail:dfalceta@usp.br

© 2014 RAS

internal shock (IS) scenario, magnetic fields are assumed not to play dynamically any major role, i.e. $\sigma \ll 1$. An alternative view is that the GRB outflow is powered by magnetic extraction from the rotational energy of a massive star or an accreting black hole and therefore, carries a dynamically important magnetic field component, i.e. $\sigma \gg 1$. The GRB radiation in this case would be powered by dissipation of the magnetic field energy in the ejecta (e.g. Usov 1992; Thompson 1994; Meszaros & Rees 1997; Piran 1999, 2005; Lyutikov & Blandford 2003; Zhang & Yan 2011). Even in a matter dominated outflow where the magnetic field does not influence the dynamics, magnetic fields play a crucial role at the radiation emission region. Magnetic fields dominate the process of particle acceleration in the collisionless shocks and also play an important role on the afterglow synchrotron emission.

Another important aspect related to magnetically dominated (large σ) jets is that observations require that they become matter dominated at some point beyond the central engine, with the conversion of the energy transported outward in the form of Poynting flux into kinetic energy flux. The mechanism by which this occurs is not known yet. It could be related to gradual acceleration of the flow (Heyvaerts & Norman 1989; Chiueh et al. 1991; Bogovalov 1996; Lyubarsky 2009), or to impulsive acceleration (Granot et al. 2011; Granot 2012), or even to non-ideal MHD effects such as magnetic reconnection (Lyutikov & Blandford 2003; Giannios & Spruit 2006; Lyubarsky 2010; Zhang & Yan 2011; McKinney & Uzdensky 2012; Levinson & Begelman 2013), or magnetic kink instabilities (Giannios & Spruit 2006; Levinson & Begelman 2013). This has been known as the σ problem and more recent analytical and numerical studies suggest that this conversion may occur even before the jet breaks out from the stellar envelope (Levinson & Begelman 2013; Bromberg et al. 2014; Beniamini & Piran 2014).

The ejecta can be parametrized by ϵ_B and ϵ_e which give the ratios of magnetic and kinetic energies with respect to the total energy density of the ejecta, respectively. Typical values derived from the synchrotron emission assuming approximately energy equipartition between the relativistic electrons and the magnetic field range from $\epsilon_B = 10^{-5}$ to 10^{-2} (Waxman 1997; Galama et al. 1999; Yost et al. 2003; Li & Zhao 2011; Santana et al. 2014). In general, both parameters are assumed to remain constant in the afterglow region.

In the extreme case mentioned above that the magnetically dominated flow dissipates most of its magnetic energy before the breakout of the stellar envelope (Bromberg et al. 2014; Beniamini & Piran 2014), no significant magnetic field from the source will be carried out by the external shock that produces the afterglow emission. This implies that only the ambient magnetic fields swept and compressed by the ejecta will be available to accelerate the relativistic particles responsible for the synchrotron radiation.

On the other hand, even assuming that the ejecta drags most of the magnetic field from the source, Medvedev & Loeb (1999) considered the magnetic field of a strongly magnetized compact object with $B \sim 10^{16}$G and found that it cannot account for the magnetic fields observed in the afterglow. The average field intensity over the emitting region scales as $\bar{B} \propto r^{-2}$. Therefore, one expects $B \sim 10^{-4}$ G and $\epsilon_B \sim 10^{-7}$ at the afterglow emission, about 10^{16} cm away from the source.

Other mechanisms were proposed in the literature in order to explain the origin of the magnetic field in the afterglows of GRBs in a matter dominated scenario. Most of them based on the growth of non-linear instabilities, such as the Weibel instability (Medvedev & Loeb 1999; Nishikawa et al. 2004; Hededal et al. 2004). This instability has its origin in the shock of two different populations of collisionless plasma particles. The diffusion of part of the populations into each other generates an anisotropy in the momentum distribution. The magnetic field amplification arises in order to isotropize the momentum distribution (Medvedev & Loeb 1999). Small fluctuations of the magnetic field deflect the particles by the Lorentz force leading to the generation of currents and the magnetic field increases. The deflections become stronger as the magnetic field increases generating a runaway process. In such instability, however, the amplified magnetic field is randomly oriented at very short correlation lengths ($> \delta$), where δ is the plasma skin depth $\delta = c/\omega_p$ (ω_p is the plasma frequency), in spite of the observed correlation lengths $l_{\rm corr} \sim 10^{10}\ \delta$ (Waxman 2006). Particle-in-cell (PIC) simulations have been performed in order to study this problem. For instance, Kazimura et al. (1998) found that about 5 % of the flow kinetic energy is converted into magnetic energy. Also, as pointed above, Nishikawa et al. (2003, 2004) showed that the Weibel instability amplifies non-uniform small scale magnetic fields only. This could give origin to a jitter spectra instead of a Synchroton radiation. Frederiksen et al. (2004) and Hededal et al. (2004) showed that the magnetic field amplitudes necessary to accelerate particles could be provided by this instability even in the case of a very weak upstream magnetic field, but these fields would still be small scale ones. It is quite clear that such small scale process is unable to provide the large scale and strong magnetic fields as needed to explain the afterglow emission.

As stressed before, in a matter dominated scenario, we are left with the ambient magnetic fields. The magnetic energy density increases due to the shock compression of the interstellar medium (ISM), which can be derived analytically from the one-dimensional relativistic Rankine-Hugoniot (RH). For an adiabatic shock, the RH relations predict amplification factors of $\sim \Gamma$, being Γ is the Lorentz factor (Kennel & Coroniti 1984; Appl & Camenzind 1988; Summerlin & Baring 2012). Typical magnetic fields in the ISM of a few μG imply $\epsilon_B \sim 10^{-11}$ (Medvedev & Loeb 1999). However, when considering the confinement of the magnetized expanding flow between the forward bow shock and the reverse shock the amplification of the magnetic fields is more efficient, as also qualitatively evidenced in former numerical studies of non-relativistic and relativistic jets (e.g. Leismann et al. 2005). A systematic study of the magnetic field evolution and amplification in such systems, sweeping a vast parametric space, is still missing though.

In this work, we revisit the problem of the magnetic field amplification behind the shocks of GRBs. The paradigm considered here for the afterglow emission is that described e.g., in Granot & Kronigl (2001):

In the case of GRB afterglows, the most common interpretation is in terms of shocks that form at the interface between the relativistically outflowing material and the surrounding medium (with the bulk of the observed emission

arising in the "forward" shock that propagates into the ambient medium...). The radiation is inferred to be nonthermal, with the dominant emission mechanisms most commonly invoked being synchrotron and inverse Compton.

In this context, we study numerically the time evolution of the magnetization in the shocks generated by a relativistic jet. We adopt the matter dominated outflow scenario and explore the amplification of ambient magnetic fields at the shocks by means of two-dimensional (2D) relativistic magnetohydrodynamics (RMHD) numerical simulations. Our goal is to study whether the resulting compressed fields behind the shocks are sufficient to explain the observed afterglow emission without requiring a magnetically dominated flow scenario.

We study different possible scenarios. Specifically, we consider the expansion of conical jets with different opening angles, from $\theta = 0$ (cylindrical case) up to 20°, before and after they break out from the stellar envelope expanding over the interstellar gas with either smaller or larger densities than the later.

The paper is organized as follows. In Section 2 we review the basic jump conditions in RMHD shocks. In Section 3 we describe the numerical setup and the RMHD equations to be solved numerically in two-dimensions (2D). In section 4 we describe the numerical results from the simulations and show the magnetic field amplification due to shock compression and pile-up behind the shocks at the jet head. In Section 5 we study the coherence length of the magnetic field using structure functions and compare them with other proposed mechanisms of magnetic field amplification. Finally, in Section 6, we discuss our results and the implications for GRB jets and draw our conclusions.

2 RELATIVISTIC SHOCKS

In the most simplified analytical model, a shock is considered a single discontinuity separating the upstream and downstream media. If considered at the reference frame of the shock front, the steady state form of the fluid equations (i.e. $\partial_t = 0$) provides the Rankine-Hugoniot jump conditions for the downstream. The relativistic jump conditions for a magnetized case (with the shock velocity normal to the magnetic field direction) are well described in Kennel & Coroniti (1984) (see also de Hoffmann & Teller 1950; Mallick 2011). Here we use the same notation to describe a shock with velocity perpendicular to the magnetic field.

$$n_1 u_1 = n_2 u_2, \tag{1}$$

$$E = \frac{u_1 B_1}{\Gamma_1} = \frac{u_2 B_2}{\Gamma_2}, \tag{2}$$

$$\Gamma_1 \mu_1 + \frac{E B_1}{4\pi n_1 u_1} = \Gamma_2 \mu_2 + \frac{E B_2}{4\pi n_2 u_2}, \tag{3}$$

$$\mu_1 u_1 + \frac{P_1}{n_1 u_1} + \frac{B_1^2}{8\pi n_1 u_1} = \mu_2 u_2 + \frac{P_2}{n_2 u_2} + \frac{B_2^2}{8\pi n_2 u_2}, \tag{4}$$

where P is the thermal pressure, n is the number density, Γ the Lorentz factor, u is the velocity normal to the shock plane, E is the electric field in the shock frame, and B the magnetic field in the region 1 (upstream, unshocked region) and the region 2 (downstream, shocked region). The factor μ is the specific enthalpy, which for a relativistic gas with a polytropic index γ is defined by:

$$\mu = 1 + \frac{\gamma}{\gamma - 1}\left(\frac{P}{nmc^2}\right). \tag{5}$$

In the case of a relativistic adiabatic shock $\gamma \to 4/3$.

From the set of equations (1-5) above the magnetic amplification ratio B_2/B_1 is obtained:

$$Y \equiv \frac{B_2}{B_1} = \frac{N_2}{N_1} = \frac{\Gamma_2 u_1}{\Gamma_1 u_2}. \tag{6}$$

Notice that the measured number density N relates to the proper density through the relation $N = n\Gamma$ (Gallant et al. 1992).

According to the conservation equations above, the amplification of the magnetic field occurs due to the strong shock compression. The basic assumption of a fluid frozen into the magnetic fields results in an equal jump condition for both ρ and B. Therefore, for strong shocks, part of the kinetic energy is converted to magnetic energy.

This scenario is more complex if the shocked region is bounded by two shocks. Actually, this is the case of the high speed jet propagating over the ambient medium. At the reference frame of a supersonic shock there are two incoming flows, the relativistic jet from one side and the ambient gas from the other with a contact discontinuity between them, where the kinetic linear momenta are equal. If compression leads to significant lateral expansion an outflow is expected to emerge in the direction perpendicular to the inflows (see Fig.1), and this problem cannot be solved in one dimension.

Following Fig.1, the upstream jet gas is decelerated at the shock discontinuity on the left (shock 1) and its downstream shocked material is pushed outwards in the lateral direction. The ambient material is shocked at the discontinuity on the right (shock 2), enters the shock region, and leaves outward, as well. The equilibrium of momentum between both downstream flows occurs at the contact discontinuity, and turbulent mixing of the fluids at this surface may occur.

Earlier three-dimensional (3D) numerical studies of hydrodynamical non-relativistic jets (Chernin et al. 1994) have demonstrated that this mixing depends mainly on the jet Mach number and the density ratio between the jet and the ambient gas. For small values of both parameters (Mach numbers < 6 and density ratios < 3) turbulent mixing and entrainment become important - a condition typically fulfilled, e.g., by certain classes of AGN jets (see e.g. de Gouveia Dal Pino & Benz 1993; Raga & Cabrit 1993; Stone & Norman 1993; de Gouveia dal Pino 2005, and references therein) and for further hydrodynamical studies (Folini & Walder 2000, 2006) (check also Cerqueira et al. 1997; Falceta-Gonçalves & Abraham 2012, for similar studies in non-relativistic MHD flows).

These authors also showed that the momentum transfer and width of the shocked region is strongly affected by the thermal radiative cooling of the shocked material. Strong cooling decreases the turbulent mixing (as part of the in-

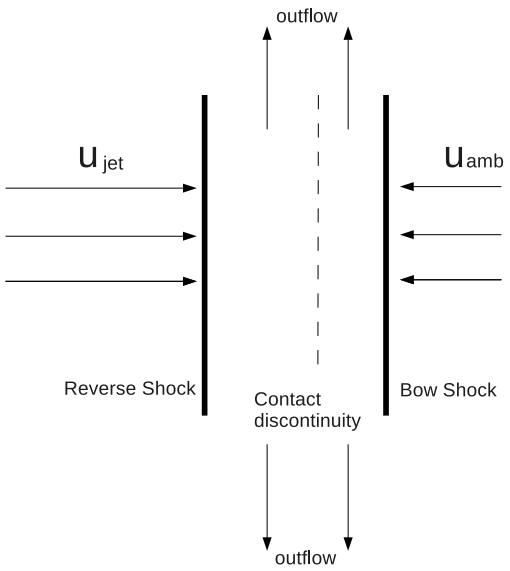

Figure 1. Idealized and simplified picture of the shock fronts generated by a relativistic jet expanding over the ambient medium at rest. Differently to what happens in an isotropically expanding blast wave, the downstream ambient material is able to flow along the contact discontinuity. This results in a lower downstream pressure and in a thinner shock front, compared to the isotropic case.

ternal energy of the shocked material is radiated away) and also shrinks the shock region, as the downstream internal energy is small compared to the upstream kinetic one. A consequence of non-uniform cooling and thin shock regions is the growth of the non-linear thin layer instability (Vishniac 1994) and the Rayleigh-Taylor instability which can break the bow shock region into a healthy clumpy structure (Blondin et al. 1990; de Gouveia Dal Pino & Benz 1993, 1994; Stone & Norman 1993).

In the case of magnetized shock-bounded slabs, the upstream gas drags field lines into the shocked region. Depending on the orientation of the upstream fields, the downstream magnetic field lines are not carried away with the outflow. 2D MHD numerical simulations of non-relativistic converging flows reveal that part of the magnetic field component perpendicular to the shock velocity $B_\perp$ is not advected, instead, it piles-up and remains parallel to the contact discontinuity surface (Falceta-Gonçalves & Abraham 2012; Falceta-Gonçalves & Monteiro 2014). Then, the downstream shocked plasma flows along the amplified field lines outwards to fill the cocoon surrounding the jet beam. Since the jet is continuously pushing the ambient gas forward there is a constant inflow of ambient magnetic field lines into the bow shock region, causing the *piling-up effect*.

If we consider the pile-up effect of the ambient magnetic field only, magnetic flux conservation implies a piled-up magnetic field intensity in the shock frame given by:

$$B_{\rm x} \simeq B_{\rm amb}\left(\frac{x_{bs}(t)}{\lambda}\right)^{\alpha}, \qquad (7)$$

where $B_{\rm x}$ is the magnetic field that is squeezed behind the shock structure after the bow shock at the jet head has propagated a distance $x_{bs}(t)$ and λ represents the width of the shock region. Here, $\alpha \to 1$ if the field is parallel to the contact discontinuity and $\alpha \to 0$ if the field lines are mostly perpendicular to the discontinuity. Fig.2 sketches the pile-up effect. The arrows represent an initially uniform magnetic field in the ambient medium and as the jet propagates it sweeps the magnetic field lines which are compressed within the double shock structure, i.e., between the forward bow shock and the reverse jet shock.

An analytical estimate of λ is not trivial though, mostly because of the asymmetric morphology of the shock region. The shock thickness for spherical relativistic blast waves has been derived as $\lambda \sim R/\Gamma$ (Blandford & McKee 1976), being R the shock wave radius. Since $R = R(t)$, the thickness λ is also a function of time. This expansion of λ with time may be understood from the conservation of matter and energy. The shock dynamics is that of a one-dimensional radial Riemann problem, but with an uniformly expanding shocked volume as the shell expands. The accumulation, as the blast wave moves, results in local increase of enthalpy that leads to an expansion of the shock thickness.

This scenario is different for the jet case though, which is not well-described by an one-dimensional Riemann problem. Here the shocked gas flows away from the axis of symmetry. If a steady state is achieved and if the jet is collimated into a quasi-cylindrical shape, i.e. $\theta \to 0$, there is no net enhancement of local enthalpy and λ is constant with time. In this case, by considering mass conservation at the dashed area of Fig.2 one obtains, for the $\theta \to 0$ (cylindrical) case:

$$\lambda_{\rm cyl} \simeq \frac{r_{\rm jet}}{2}\frac{n_{\rm j,1}u_{\rm j,1} + n_{\rm A,1}u_{\rm sh}}{n_{\rm j,1}Y_{\rm j}u_{\rm j,2} + n_{\rm A,1}Y_{\rm A}u_{\rm A,2}} \qquad (8)$$

where $r_{\rm jet}$ represents the radius of the jet at the working surface, Y the jump in density between downstream and upstream flows, indices j and A account for jet and ambient values, respectively, and $u_{\rm sh}$ represents the speed of the shock region in the observers reference frame: [1]

$$u_{\rm sh} \sim u_{\rm j,1}\frac{\left(n_{\rm j,1}\Gamma_1^2 n_{\rm A,1}^{-1}\right)^{1/2}}{1+\left(n_{\rm j,1}\Gamma_1^2 n_{\rm A,1}^{-1}\right)^{1/2}}. \qquad (9)$$

Since in the case of a well-collimated (cylindrical) jet $r_{\rm jet}$ is constant as the shock front moves further away of the central source, for $\Gamma_1 \gg 1$, we obtain:

$$\lambda_{\rm cyl} \sim \frac{\sqrt{2}}{2}\eta r_{\rm jet} \qquad (10)$$

where $\eta = n_{\rm A,1}/n_{\rm j,1}$.

[1] which is obtained from momentum flux conservation assuming that the ambient pressure is negligible, as the gas is cold, and the jet pressure is much smaller than the jet shock ram pressure

As discussed later on in the paper, there are observational evidences - as well as results from numerical simulations - indicating that core-collapse GRB jets may be, in reality, not well collimated after the breakout of the stellar envelope. Observationally, power-law break decay during the afterglow emission has been well modelled by means of conical jets, with opening angles as large as 20°, being $\theta_{\rm j} < 10^\circ$ in a vast majority of objects (see Sari et al. 1999; Bloom et al. 2003; Frail et al 2001; Zeh et al. 2006; Tchekhovskoy et al. 2009; Bromberg et al. 2011; Mizuta & Ioka 2013).

In the case of a conical jet the rate at which gas is loaded into the shock region varies with time. This because the Mach disk, i.e. the area of the jet working over the shocked gas, increases as the jet propagates forward, away from the central source. To obtain a modified analytical approximation for this case, we separate the fluxes of gas into the shock region in two, one being exactly the same as considered in Eq.8, and the other being the net increase due to the increased radius of the jet, i.e. $\Phi_{\rm tot} = \Phi_{r_{\rm jet,0}} + \Phi_{\Delta r_{\rm jet}}$. Let us consider a simple case in which the opening angle θ is constant. Since $\Delta r_j \propto x(t) tan\theta$, Eq.8, with now $r_{\rm jet} = r_{\rm jet}(t) = r_{\rm jet,0} + \Delta r_j$, results in:

$$\lambda_{\rm con}(t) \sim \lambda_{\rm cyl}\left(1 + \frac{x(t)\tan\theta}{r_{\rm jet,0}\Gamma_1}\right) \qquad (11)$$

Therefore, the pile-up must occur at shorter distances in the case of conical jets, with a departure from the linear growth of B and eventual saturation of the magnetic field amplification,consistent with causality constraints.

Using Eqs.7 and 11, we computed the pile-up effect which is shown in Fig.2 (bottom) as a function of the distance to the central source, for different jet parameters. We clearly see in the Figure that for large values of Γ, the difference between collimated ($\theta \to 0$) and wide jets decreases substantially.

As stated before, despite the extensive numerical multidimensional study that can be found in the literature of magnetized relativistic jet flows, a systematic study of the amplification of ambient magnetic fields by relativistic jets, particularly in the context of GRBs, is still missing. In the following sections we will explore this issue and test the scenarios above considering relativistic MHD numerical simulations of both collimated and wide jets propagating over a weakly magnetized ambient.

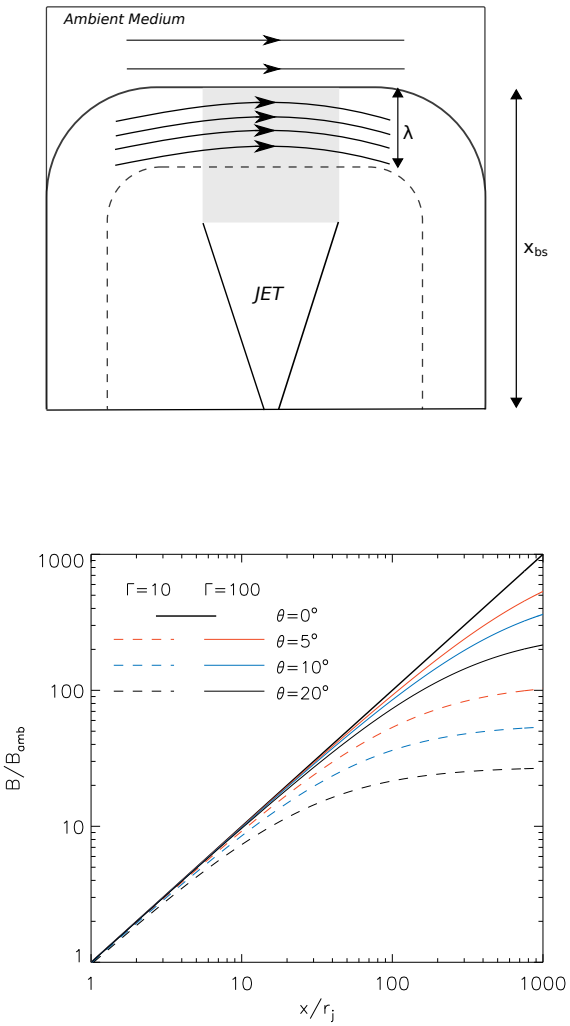

Figure 2. Up: Schematic representation of the pile-up effect of the magnetic field lines as the jet propagates in an ambient medium with uniform magnetic field. Bottom: Pile-up effect on the magnetic field intensity at the shock region for collimated and wide jets as a function of the distance, as given by Eqs.7 and 11, respectively, for different jet opening angles, and for $\Gamma = 10$ (dashed) and $\Gamma = 100$ (solid).

3 GOVERNING EQUATIONS AND NUMERICAL SETUP

The evolution of our system is governed by the special relativistic magnetohydrodynamic equations (SRMHD) which can be written in the general conservative form

$$\partial_t \mathbf{U} + \nabla \cdot \mathbf{F}(\mathbf{U}) = 0, \qquad (12)$$

where $\mathbf{U}$ is the vector of conserved variables

$$\begin{aligned}\mathbf{U} &= (D, \mathbf{S}, \mathbf{B}, E)^T \\ &= \Big(\Gamma\rho, \left(\xi + B^2\right)\mathbf{v} - (\mathbf{v}\cdot\mathbf{B})\,\mathbf{B}, \mathbf{B}, \\ &\quad \xi + \frac{1}{2}\left(B^2 + v^2B^2 - (\mathbf{v}\cdot\mathbf{B})^2\right) - p - D\Big)^T, \end{aligned} \qquad (13)$$

and $\mathbf{F}$ is the tensor of fluxes

$$\begin{aligned}\mathbf{F} &= \Big(D\mathbf{v}, \\ &\quad \left(\xi + B^2\right)\mathbf{v}\mathbf{v} - \frac{\mathbf{B}\mathbf{B}}{\Gamma^2} - (\mathbf{v}\cdot\mathbf{B})\,(\mathbf{B}\mathbf{v} + \mathbf{v}\mathbf{B}) + \mathbf{I}p_{\rm tot}, \\ &\quad \mathbf{v}\mathbf{B} - \mathbf{B}\mathbf{v}, E\mathbf{v} + p_{\rm tot}\mathbf{v} - (\mathbf{v}\cdot\mathbf{B})\,\mathbf{B}\Big)^T, \end{aligned} \qquad (14)$$

where D is the rest mass density, $\mathbf{S}$ is the momentum density, E is the energy density, ρ is the mass density, $\mathbf{v}$ is the fluid velocity, $\mathbf{B}$ is the magnetic field, $p_{tot} = p + p_{\rm mag}$ is the total pressure, p is the gas pressure, $p_{\rm mag} = \frac{1}{2}\left((B/\Gamma)^2 + (\mathbf{v}\cdot\mathbf{B})^2\right)$ is the magnetic pressure, $\Gamma = \left[1 - (v/c)^2\right]^{-1}$ is the Lorentz factor, and for the case of an ideal equation of state with a constant polytropic index γ, the measure of enthalpy ξ is given by

$$\xi = \Gamma^2\left(\rho + \frac{\gamma}{\gamma - 1}p\right). \qquad (15)$$

The above set of equations was solved using the GODUNOV code (check *http://amuncode.org* for the public available source code) which implements the Godunov-framework of the hyperbolic equation numerical solution (Godunov 1959) extended by methods suitable to solve the SRMHD equations. The code has been extensively tested and applied to several astrophysical problems (e.g. Kowal & Lazarian 2010; Falceta-Gonçalves et al. 2010a,b,c; Santos-Lima et al. 2010; Kowal et al. 2011a,b, 2012; Santos-Lima et al. 2012, 2013; Poidevin et al. 2013) In the work presented here we used the 5^{th} order monotonicity-preserving (MP) reconstruction (Suresh & Huynh 1997; He et al. 2011) of the Riemann states, the approximate HLLC Riemann solver (Mignone & Bodo 2006) in order to calculate the numerical approximation of the fluxes $\mathbf{F}$. The solution advances in time using the 3^{rd} order four-stage explicit optimal Strong Stability Preserving Runge-Kutta SSPRK(4,3) method (Ruuth 2006). In order to keep the divergence of magnetic field minimum, we use the hyperbolic divergence cleaning approach by Dedner et al. (2002).

A non-straightforward element of the solution of the relativistic MHD equations is the determination of the primitive variables $\mathbf{Q} = (\rho, \mathbf{v}, \mathbf{B}, p)$ from their conservative representation $\mathbf{U}$ (see Eq. 13). While in the non-relativistic case the conversion requires only simple algebraic manipulations, here we are forced to use iterative methods. A number of such methods has been compared in Noble et al. (2006) with the conclusion that their 1Dw scheme is the most accurate and robust one and therefore, it is also employed in our calculations.

3.1 Initial setup

Significant progress has been achieved in the past years regarding relativistic jet simulations both in the framework of extragalactic jets (Marti et al. 1997; Aloy et al. 1999; Hughes et al. 2002) and of GRB jets (Komissarov 1999; MacFadyen et al. 2001; Zhang et al. 2003; Leismann et al. 2005; Tchekhovskoy et al. 2010, 2008; Morsony, Lazzati & Begelman 2007; Mizuta & Aloy 2009; Lazzati et al. 2009; De Colle et al. 2012; Mizuta & Ioka 2013; Bromberg et al. 2014), most of which were performed in the low σ regime and, due to computational limitations, in two-dimensions[2], but none focussed on the investigation of the interaction of the shocks of the ejecta with the ambient magnetic field after the breakout of the collapsing stellar envelope.

There is some debate in the literature regarding the GRB jet opening angle at the breakout (see e.g. Lazzati & Begelman 2005; Morsony, Lazzati & Begelman 2007; Tchekhovskoy et al. 2008; Mizuta & Ioka 2013; Bromberg et al. 2014, and references therein). When inside the stellar envelope, collimation of a Poynting flux-driven jet may occur due to net currents driven locally, as well as by the surrounding pressure. The energy dissipation at the jet shock head increases the total pressure of a hot cocoon that develops around the jet which helps collimating the jet. Once the jet breaks out of the stellar envelope, it may become wider due to reduced pressure (Bromberg et al. 2011; Mizuta & Ioka 2013). There is in fact evidence in favour of conical jets. Tchekhovskoy et al. (2009), for instance, finds from his simulations Lorentz factors $\Gamma \sim 100 - 5000$ and opening angles $\theta_{\rm j} \sim 0.1 - 10^{\circ}$, reproducing inferred properties of GRB jets. On the other hand, the confinement inside the envelope of a Poynting flux dominated jet due to both magnetic and cocoon pressure can be so large that the jet can emerge from the stellar envelope with a radius of the order of the source light cylinder radius (R_L) and likely remain confined well after the breakout providing a consistent jet scenario for both the prompt gamma emission and the formation of a photosphere (Levinson & Begelman 2013).

Observationally, the opening angle is inferred by fitting the break in the power-law decay of the afterglow emission with the fluxes expected from an emitting plasma subject to relativistic beaming (Rhoads 1999). The fit model depends on several simplifications, such as the density distribution of the surrounding medium (e.g. for winds or ISM), and radial dependencies within the jet. Under these conditions, the vast majority of GRBs data results in $\theta_{\rm j} < 10^{\circ}$, with fiducial estimates at $\theta_{\rm j} \sim 4^{\circ}$ (Sari et al. 1999; Bloom et al. 2003; Frail et al 2001; Zeh et al. 2006).

While this question of the jet opening angle is still debatable (e.g. Lazzati & Begelman 2005; Morsony, Lazzati & Begelman 2007; Tchekhovskoy et al. 2009; Bromberg et al. 2014), in this work we explore different possible values for this parameter. At the inlet of the computational domain we start with a jet that has just emerged from the collapsing stellar envelope into the ambient medium. For the sake of simplicity the jet in our simulations is not launched from first principles, but injected as boundary condition. The opening angle is therefore a free parameter and in our simulations three conditions have been tested for it, namely $\theta_{\rm j} = 0^{\circ}$,$10^{\circ}$ and 20°. Also, $\theta_{\rm j}$ is set as constant as the jet emerges from the collapsing stellar envelope into the ambient medium.

The initial setup of the jet beam is built with a region of continuous injection of material into the computational domain of radius $R_{\rm j}$, which defines the jet radius, set at the left vertical boundary of the box domain. The bottom horizontal and the left vertical boundaries of the box are assumed to be reflective, while the other are open boundaries allowing the material to leave the domain.

The ambient gas density ρ and pressure p are assumed initially uniform in the whole domain. Since we are interested in the study of the amplification of the magnetic field in the shock region of a matter dominated flow, we set a weak uniform ambient magnetic field initially perpendicular to the propagation of the jet, corresponding to $P_{mag}/P_{th} = 10^{-5}$.

Another important parameter for the dynamical evolution of jets, though not critical for the purpose of this work as we discuss further below in the paper, is the ratio between the surrounding ambient and the jet densities ($\eta = \rho_{\rm amb}/\rho_{\rm jet}$). Traditionally, relativistic jet propagation models for microquasars, AGNs and GRBs assume an underdense relativistic flow, i.e., with a density smaller than that of the ambient medium. One of the justifications for

[2] The 2-dimensional approach in this work means that the system is considered in a planar symmetry, not axial, since the external magnetic field has to be kept uniform. Such approach is limited, obviously, and underestimates the dynamics of the flows perpendicular to the plane, i.e. ortogonal to the magnetic field. A more detailed discussion about this is presented later in the manuscript, but a more comprehensive picture will be provided in a future work where a full 3-dimensional modelling is presented.

this assumption is the general absence of thermal emission in the shocks of these jets. In the collapsar scenario, if the GRB jet is magnetically driven, the launch occurs probably with $\eta > 1$ (see e.g. simulations by López-Cámara et al. 2013), as predicted by the semianalytical models and numerical simulations referenced in the previous sections. After breaking out of the envelope, far from the stellar material, the jet may change its mass regime and the jet density may become larger than that of the ambient, i.e. $\eta \ll 1$. This is discussed, for instance, by Lazzati & Begelman (2005) and Morsony, Lazzati & Begelman (2007). Simulations of the jet-envelope interaction indicate a transition between the regimes of $\eta \simeq 10^4 - 10^5$ (at the central region of the stellar envelope) and $\eta < 10^{-6}$ after the jet breaks the outer boundary of the star.

Since the dynamical evolution of the jet over an uniform ambient medium may differ considerably depending on the parameter η chosen, for the sake of completeness, we studied the dynamical evolution of jets in both regimes, i.e. $\eta < 1.0$ and $\eta > 1.0$, sweeping a parametric range $10^{-4} \leqslant \eta \leqslant 10^2$. In this sense we can study the different morphologies and magnetic field amplification for the phases of the jet interacting with the surrounding media right after the breakout of the stellar envelope and further out.

The space of parameters investigated in this work is presented in Table 1. In all cases the jet is initially relativistic (with Lorentz factors $\Gamma = 2$, 10, or 100) and supersonic, i.e. the initial Mach number, defined as $M \equiv v_{\rm jet}/c_s$ is set as 10 for all models, where the sound speed is given by $c_s = \sqrt{\gamma\,(\gamma-1)\,P/\left[(\gamma-1)\,\rho + \gamma P\right]}$.

The dimensions of the simulated computational box is $(L_x, L_y) = (48, 12)$ in code units. The adopted code unit for the distance is $5R_j$. The code unit for time is defined as $5R_j/c$, where c is equal 1 in our simulations. The simulations were performed with a resolution of 4096×1024 cells.

The thermal radiative cooling of the hot shocked ambient plasma may result in thin and unstable shock regions. However, radiative losses of GRB jets are dominantly non-thermal, mainly synchrotron and inverse-Compton processes. The actual role of these processes in the cooling of the shocked plasma at the afterglow phase is not clear yet (Granot & Konigl 2001). For this reason, we run most of our models under an adiabatic regime ($\gamma = 4/3$) and, in order to mimic the action of the thermal radiative cooling at the bow shock region upon the magnetic field amplification, we run the same models with a reduced effective polytropic index of $\gamma = 1.1$ (these models are referred as *NA* in Table 1).

Notice that we have used an uniform value of γ for the whole computational domain. Recent works have focused on the stability and thermodynamical aspects that can influence the jet dynamics (Bodo et al. 2013). Mignone & McKinney (2007) explored the effects of varying smoothly the gas enthalpy in the propagation of a relativistic jet (with an polytropic index $\gamma = 4/3$) into a non-relativistic medium (with $\gamma = 5/3$). [3] Their two-dimensional simulations revealed a slower evolution of the jet and changes in the shape of the cocoon, but the main conclusion was that the overall structure of the relativistic jet with the modified enthalpy equation is similar to the case with uniform $\gamma = 4/3$.

The simulations were run until the propagating jet reached the right vertical boundary of the computational domain, except for the model with Lorentz factor $\Gamma = 2$, for which the jet power was too little to drill the ambient gas through to the right boundary. The outcomes of the simulations are described in the following section.

[3] Long before Taub (1948) had shown that in order to preserve the consistency with the relativistic kinetic theory, the specific enthalpy μ has to satisfy the inequality: $(\mu - \Theta)(\mu - 4\Theta) \geqslant 1$, where $\Theta = p/\rho$ and μ is the enthalpy of the relativistic gas and their proposed equation of state satisfies the Taub inequality.

Table 1. Parameters used in each simulation run. We explore the dependence with the density ratio, polytropic index, Lorentz factor and opening angle. The angle equal 0° refers to the case where the jet is injected with a cylindrical geometry.

γ	Mach	Γ	$\rho_{\rm amb}/\rho_{\rm jet}$	$\theta_{\rm j}$	*Model*
1.1	10	2	10^2	0°	NA1cyl
1.1	10	10	10^2	0°	NA2cyl
1.1	10	100	10^2	0°	NA3cyl
1.33	10	2	10^2	0°	AD1cyl
1.33	10	10	10^2	0°	AD2cyl
1.33	10	100	10^2	0°	AD3cyl
1.33	10	10	10	0°	AD4cyl
1.33	10	10	1	0°	AD5cyl
1.33	10	10	10^{-4}	0°	AD6cyl
1.33	10	10	10^{-2}	0°	AD7cyl
1.33	10	10	10^{-3}	0°	AD8cyl
1.33	10	100	10^{-4}	0°	AD9cyl
1.1	10	10	10^2	10°	NA1con
1.1	10	100	10^2	10°	NA2con
1.33	10	10	10^2	10°	AD1con
1.33	10	100	10^2	10°	AD2con
1.33	10	10	10^{-4}	10°	AD3con
1.33	10	100	10^{-4}	10°	AD4con
1.33	10	10	10^{-4}	20°	AD5con
1.33	10	100	10^{-4}	20°	AD6con

4 NUMERICAL RESULTS

In this section we present the results from the simulations and comparisons between the different models.

4.1 Jet/Ambient morphologies

4.1.1 $\eta > 1.0$ (light jets)

Let us first discuss the morphologies of the shocked material surrounding light jets. These models can be specially suitable for right after the breakout of the jet into the environment of the core-collapse GRB.

In Fig.3 we present snapshots of the density distribution for the adiabatic ($\gamma = 4/3$) (left column) and non-adiabatic ($\gamma_{\rm eff} = 1.1$) (right column) models of Table 1 with different Lorentz factors and jet opening angles.

All models evidence the formation of a bow shock structure as the jet head sweeps the ambient gas. The ambient shocked material is deposited into a cocoon that surrounds the beam. Although not obvious in the snapshots shown in Fig.3, a double shock structure soon develops. Besides the forward bow shock, a reverse internal shock decelerates the

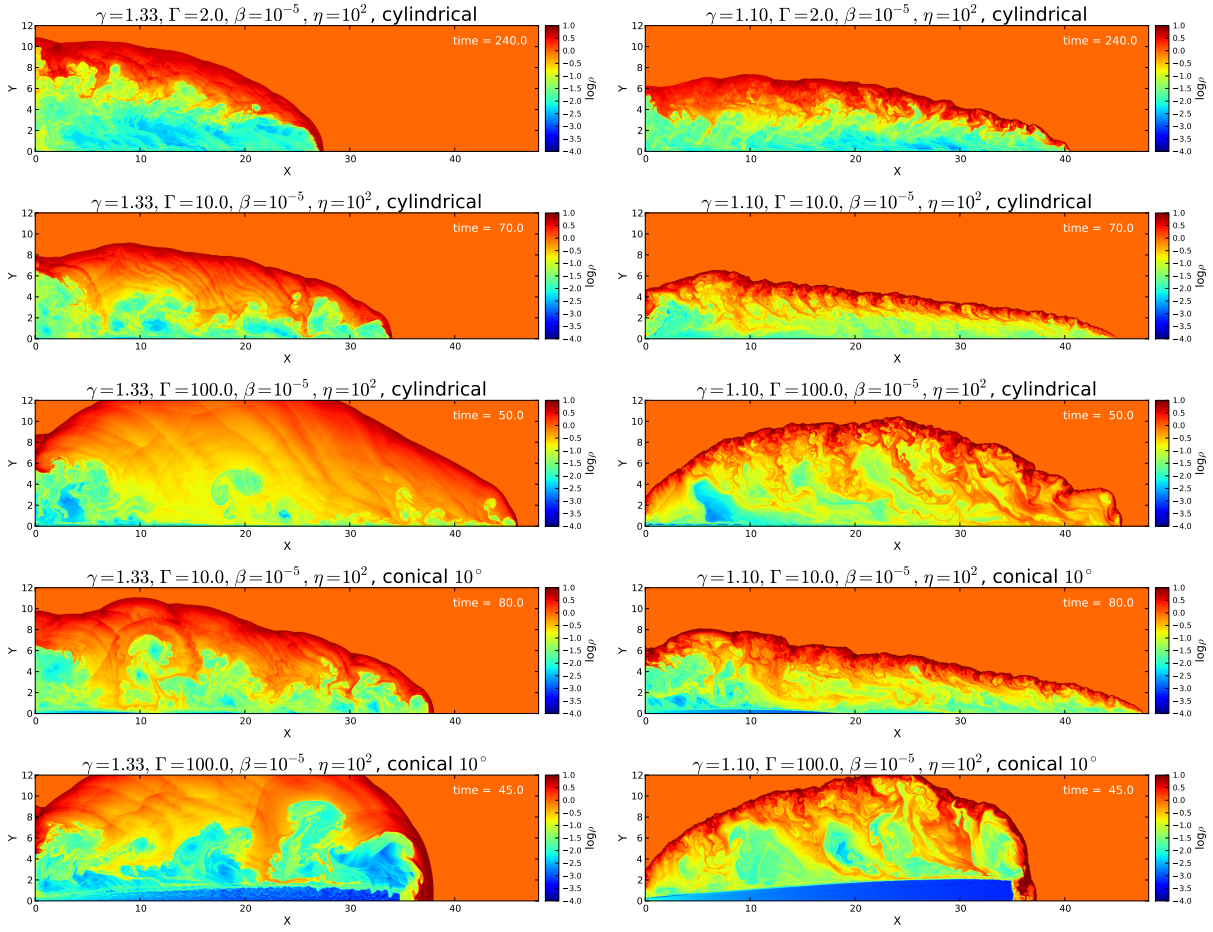

Figure 3. Distribution of logarithm of density for different light jet models with $\eta = 10^2$. Left column maps represent adiabatic ($\gamma = 4/3$) simulations and the non-adiabatic ($\gamma_{\rm eff} = 1.1$) models are shown in the right column. Models were run with $\Gamma = 2$, $\Gamma = 10$ and $\Gamma = 100$ and the geometry was tested both for collimated ($\theta \rightarrow 0$) and wide jets. Numbers represent the time of the given snapshot in the simulation in code units.

jet beam and shocked jet material is also deposited into the internal part of the cocoon. The low density portion of the cocoon is of jet shocked material, while the denser one is composed of shocked ambient gas.

The interaction of the hot shocked gas of the cocoon with the beam material drives Kelvin-Helmholtz (KH) instabilities (e.g. Birkinshaw 1996) which in turn induce both the formation of internal shocks pinching the beam and strong turbulent mixing and entrainment, as detected in former numerical studies of non-relativistic jets (de Gouveia Dal Pino & Benz 1993; Chernin et al. 1994).

Also, as expected from earlier studies of thermal radiative cooling jets (e.g., Blondin et al. 1990; de Gouveia Dal Pino & Benz 1993), the effects above are much stronger in the adiabatic jets (in the left panels of Fig. 3) since in these cases the internal energy of the shocked material in the cocoon is much larger than in their non-adiabatic counterparts (in the right side of the Fig.3). In the latter cases, the enthalpy of the gas in the cocoon is much smaller due to the adoption of a $\gamma = 1.1$ index to mimic thermal radiative cooling in the shocked dense ambient gas.

We should remark that in a more realistic calculation the effective value for γ would be dependent on the local properties of the plasma, and the cooling function. The adoption of a single value of $\gamma = 1.1$ for the whole system in the case of the right side models of Fig. 2 is, therefore, a simplification and the comparison with the adiabatic models should be taken with caution. These non-adiabatic models actually represent extreme examples.

Models with higher Lorentz factor obviously reach the boundary of the spatial domain earlier and therefore, look less evolved. The higher propagation velocity results a smaller loading of shocked jet material and larger spreading of the shocked ambient gas into the cocoon, which makes the driving of shear KH instabilities and turbulent entrainment less prominent than in lower Lorentz factor jets.

The models with smaller Lorentz factor ($\Gamma = 2$), specially the adiabatic one ($\gamma = 4/3$), present a cocoon with a larger portion of low density shocked jet gas and smaller portion of high shocked ambient gas. This is because the jet beam has not enough power to drill through the dense ambient gas and also retains much more shocked jet material.

In the non-adiabatic models, the bow shock layer is thinner. The high velocity of the upstream jet flow interacting with a thin layer gives rise to the Vishniac instability (Vishniac 1994) which breaks the layer and enhances the growth of turbulence, particularly in the outer parts of the cocoon. It is also clear in these models the impact of the tur-

bulence on the diffusion and mixing of the gas in the shocked plasma.

The morphology and general properties of the density distributions, as described above, do not differ much for conical jets. This is expected since the cocoon pressure readily becomes important in the case of these low density jets, i.e. with $\eta < 1$, resulting in similar dynamics once the jet is collimated by the cocoon.

The maximum density at the shock region is also dependent on the parameters γ and Γ. Fig. 3 indicates that larger Lorentz factors result in larger shocked densities which is consistent with the relativistic RH jump conditions (see eqs. 1 to 4). Also, the effective thermal radiative cooling introduced in the non-adiabatic jets by decreasing γ to 1.1 is expected, according to the jump conditions, to increase the density of the compressed shocked material at the same time that it decreases its internal pressure. The pressure reduction of the downstream gas also decreases the velocity at which it is pushed outwards. All these effects are detected in Fig.3 and are compatible with earlier studies of non-relativistic radiative cooling jets (Blondin et al. 1990; de Gouveia Dal Pino & Benz 1993; Stone & Norman 1993). We show in Fig.5 the Lorentz factor, density and magnetic field amplification factor at the jet axis, along y=0, for models with $\eta = 10^{-2}$.

4.1.2 $\eta < 1.0$ (heavy jets)

After the jet breaks the stellar envelope it may expand over an underdense interstellar medium. In this case, the jet density may eventually become orders of magnitude larger than that of the ambient gas. Numerical issues constrain the density contrast of the simulations, which has been fixed here to a minimum possible value $\eta = 10^{-4}$. The larger density of the jet makes it easier to expand over the ambient medium, thus reducing and delaying certain shock effects, such as the development of a large pressure cocoon.

We can see in Fig.4 that the morphology of the jet changes substantially with the increase in the jet density. For very dense jets the ambient pressure is negligible and have little impact on the propagation of the jet. The shock region shows less turbulence compared to the low density jets.

Fig.6 depicts the Lorentz factor, density and magnetic field amplification factor at the jet axis, along y=0, for models with $\eta = 10^{4}$.

The comparison of Figs.5 and 6 (see also Figs. 3 and 4) indicate that the density amplification in the interface between the cocoon and the external medium is larger with increasing density ratio η. An important fact is that for $\eta \gg 100$ the jet is too light and has little momentum to push the ambient gas. In this case the jet decelerates quickly and does not evolve to larger radii, as already pointed out in Marti et al. (1997).

In the next subsection we will see in detail how these parameters affect the spatial distribution of the magnetic field.

4.2 Magnetic Energy

The simulated jets are initially non-magnetized, while the ambient medium is weakly magnetized, therefore the magnetization of the downstream shocked gas is mostly due to the ambient field dragged into the shock at the head and the cocoon. The spatial distribution of magnetic pressure for different models with $\eta = 10^{2}$ is shown in Fig.7.

Similarly to what is observed in the density distributions, there are striking differences in the magnetic pressure distributions of the models. For the adiabatic models (left side panels) the high intensity magnetic fields are located at the interface (or contact discontinuity) that separates the

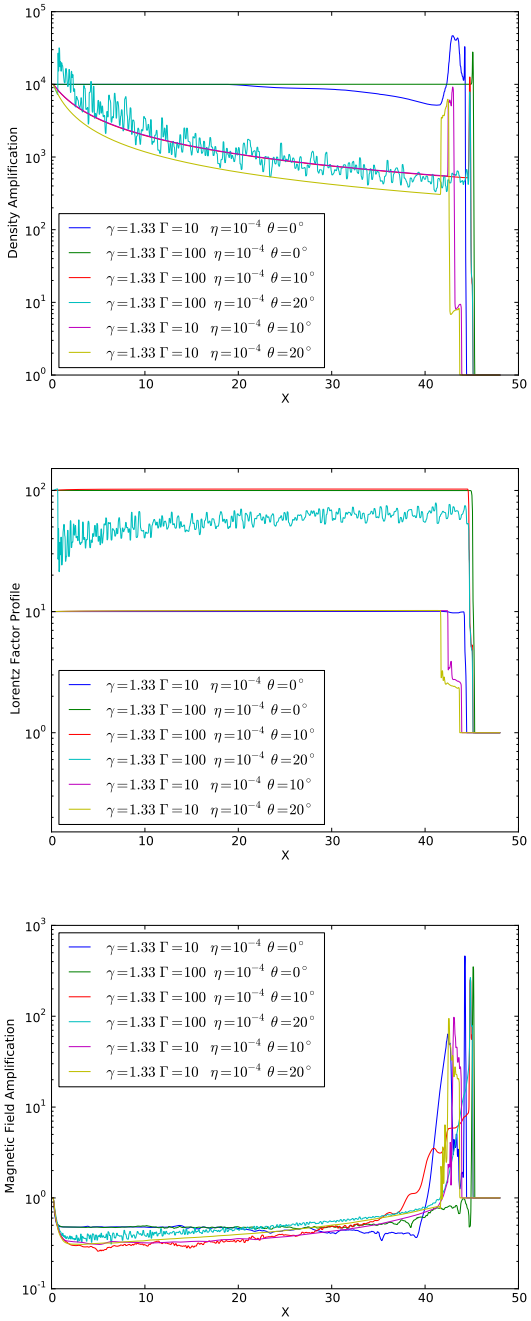

Figure 6. Profiles of the magnetic field amplification factor, the density amplification factor and the evolution of the Lorentz factor, obtained at $y = 0$, for the adiabatic ($\gamma = 4/3$) heavy jet models with $\eta = 10^{-4}$.

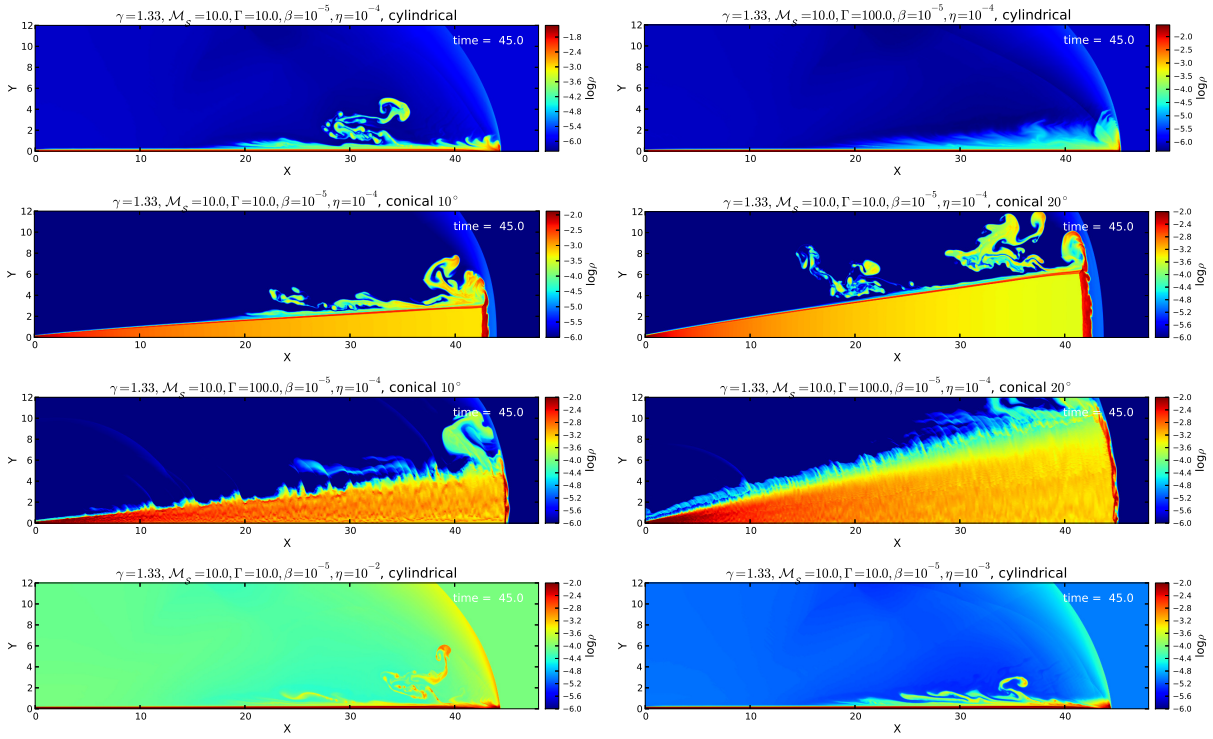

Figure 4. Distribution of logarithm of density for different adiabatic, heavy jet models (with $\eta < 1$). Models were run with $\Gamma = 10$ and $\Gamma = 100$ and the geometry was tested both for collimated ($\theta \to 0$) and wide jets, with the opening angle varying between 0°, 10° and 20°. Numbers in white represent the time of the given snapshot in the simulation in code units.

shocked jet and ambient downstream flows, (i.e., the low and high density portions of the cocoon). These high magnetic intensity regions basically contour the low density region as seen in Fig.3. The main reason for this is that the ambient magnetic field lines enter into the cocoon dragged by the shocked downstream flow. These are not able, though, to enter into the shocked jet downstream material. At the ambient downstream, the gas is deflected and flows along the contact discontinuity, as clearly seen in the adiabatic cases. The magnetic field lines, on the other hand, simply accumulate at the contact discontinuity (piling-up there). The maximum intensity of B occurs at the head of the shock for all models.

Fig.8 shows the density distribution for the well-collimated (cylindrical) jet model AD2cyl, with $\gamma = 4/3$ and $\Gamma = 10$ at $t = 90$, overplotted with five selected high intensity magnetic field lines. The streamlines depicted follow the magnetic field lines starting at the vertical coordinate $y = 12.0$ (top boundary) and horizontal coordinates $x = [11.5, 18.0, 24.5, 31.0$ and $37.5]$. The ambient region presents the initial vertical field lines. At the shock regions, the lines are deflected and stretched, as expected for a super-Alfvénic flow (i.e., with velocity higher than the local Alfvén speed). As seen in Fig.8 the field lines do not diffuse to the low density region of the cocoon. On the contrary, they accumulate at the contact discontinuity region between the ambient shocked material and the jet shocked material, where therefore, the magnetic field intensity is larger.

The comparison of the adiabatic models in the left side of Fig.7 with the non-adiabatic ones in the right hand side, indicates that the maximum values of the magnetic fields are slightly larger in the non-adiabatic cases. This is compatible with the RH jump conditions for radiative cooling flows which predict a larger density of the shocked material and therefore, a larger amplification of the magnetic field behind the shocks, than in the adiabatic counterparts.

Heavy jets ($\eta < 1$) on the other hand (Fig.9), have all similar magnetic field distributions, as already noted in the case of their density distributions. The absence of a prominent cocoon reduces the internal turbulence and its role in diffusing magnetic field lines. Nevertheless, let us perform a more careful analysis of the overall results.

The maximum magnetic energy density ($E^{\rm mag}_{\rm max}$) is generally located at the head of the bow shock region, as the jet expands. $E^{\rm mag}_{\rm max}$ as a function of the location of the bow shock head in the x-direction is shown in Fig.10. Each snapshot created from the simulations is shown as a point in the plot. The top and middle diagrams show the results for all collimated jets (with light jets being depicted in the top panel and heavy jets in the middle panel). The solid line represents the correlation $E^{\rm max}_{\rm mag} \propto x^2$, for comparison. Notice that the line is not a statistical fit, but is in good agreement with all models with $\theta = 0$. Most strikingly, all models, independent on the Lorenz factor, the polytropic index, or the density ratio η, present similar $E^{\rm max}_{\rm mag}$ at the same position of the shock head. This result is consistent with the magnetic field pile-up effect discussed in Section 2 and with Eq. 7 which predicts $B_{ampl} \propto x^{\alpha}$, with a maximum $\alpha \simeq 1$ for a compressed magnetic field parallel to the discontinuity.

In the bottom diagram of Fig.10, we show the evolution of the maximum magnetic field intensity for the conical jets.

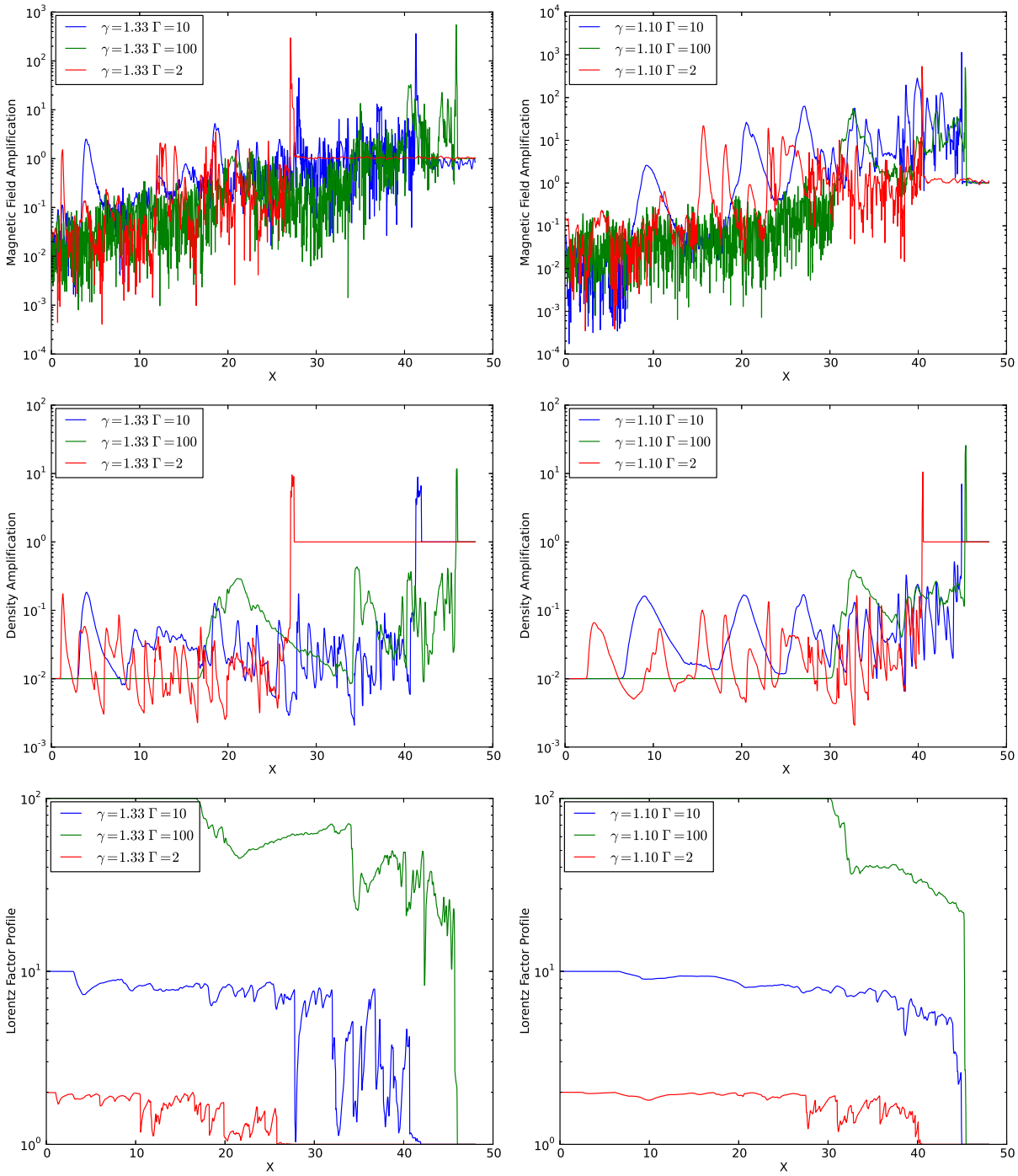

Figure 5. Profiles of the magnetic field amplification factor, the density amplification factor and the evolution of the Lorentz factor, obtained at $y = 0$, for the $\gamma = 4/3$ and 1.1 jet models, with $\eta = 10^2$.

It is clear the dependence of $E_{\rm max}^{\rm mag}$ with the opening angle θ and Γ in consistence with the analytical prediction of Eq.11.

The results above clearly show that the pile-up effect is maximized in the case of $\theta \to 0$, as one should expect. In fact, the piling-up is maximized in the forward shock region where the jet velocity is nearly normal to the magnetic field lines. Thus, although a conical geometry may offer a larger area for the forward shock to sweep the ambient magnetic lines, most of the shock front is oblique which will weaken the piling-up. Also, the net flux of plasma out of the shock region is limited (causality is not broken here), and once the Mach disk becomes large enough local enthalpy cannot be considered as constant any longer. After this transition phase the shock width scales linearly with x and the pile-up effect ceases. This is well accounted in Eq.11.

We stress here that the results obtained in Fig.10 are nearly insensitive to the jet-ambient density ratio η. This result is actually not surprising. The accumulation of the com-

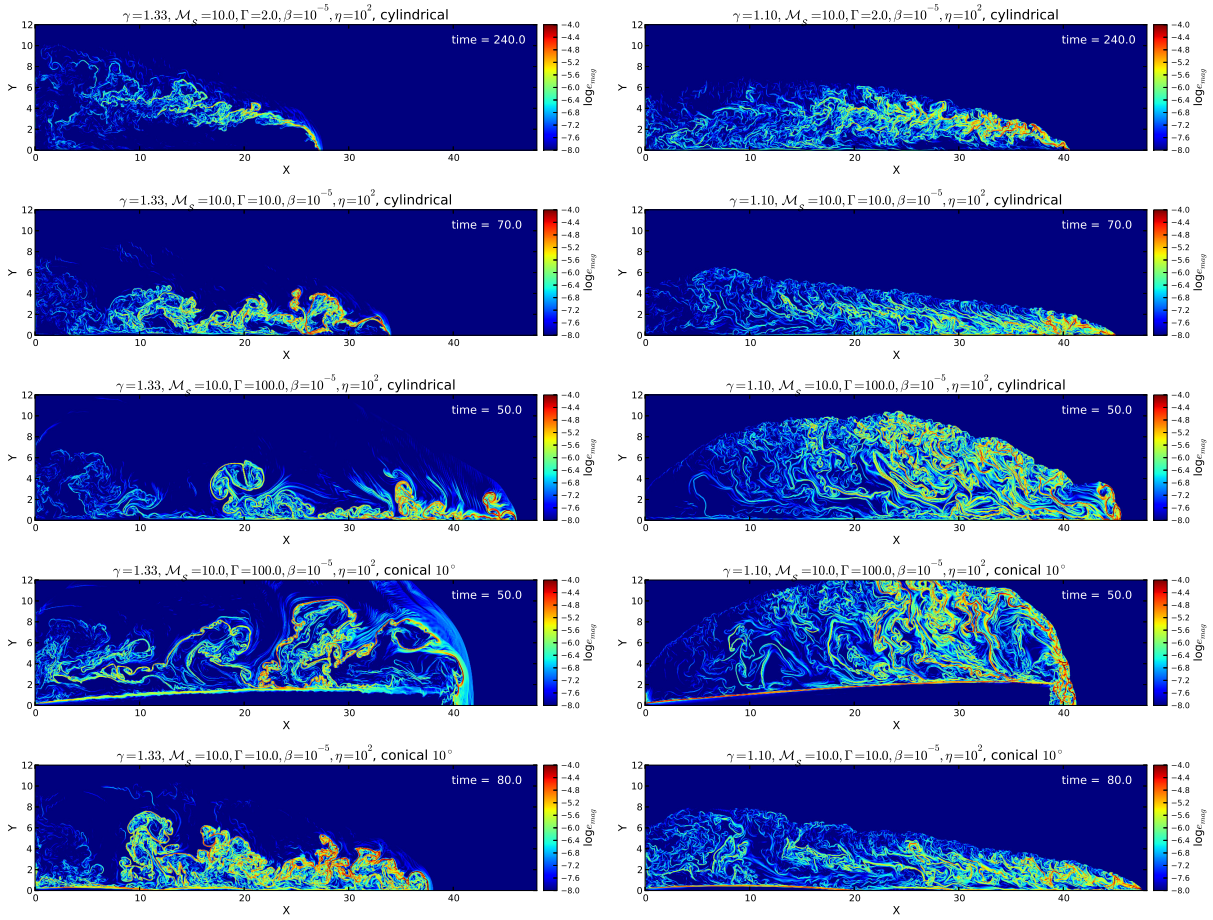
γ=1.33, M_s=10.0, Γ=2.0, β=10^-5, η=10^2, cylindrical
time = 240.0
γ=1.10, M_s=10.0, Γ=2.0, β=10^-5, η=10^2, cylindrical
time = 240.0
γ=1.33, M_s=10.0, Γ=10.0, β=10^-5, η=10^2, cylindrical
time = 70.0
γ=1.10, M_s=10.0, Γ=10.0, β=10^-5, η=10^2, cylindrical
time = 70.0
γ=1.33, M_s=10.0, Γ=100.0, β=10^-5, η=10^2, cylindrical
time = 50.0
γ=1.10, M_s=10.0, Γ=100.0, β=10^-5, η=10^2, cylindrical
time = 50.0
γ=1.33, M_s=10.0, Γ=100.0, β=10^-5, η=10^2, conical 10°
time = 50.0
γ=1.10, M_s=10.0, Γ=100.0, β=10^-5, η=10^2, conical 10°
time = 50.0
γ=1.33, M_s=10.0, Γ=10.0, β=10^-5, η=10^2, conical 10°
time = 80.0
γ=1.10, M_s=10.0, Γ=10.0, β=10^-5, η=10^2, conical 10°
time = 80.0
X
Y
log r_mag

Figure 7. Same description of Fig.3 but for the logarithm of magnetic energy density, for the jet models with $\eta = 10^2$.

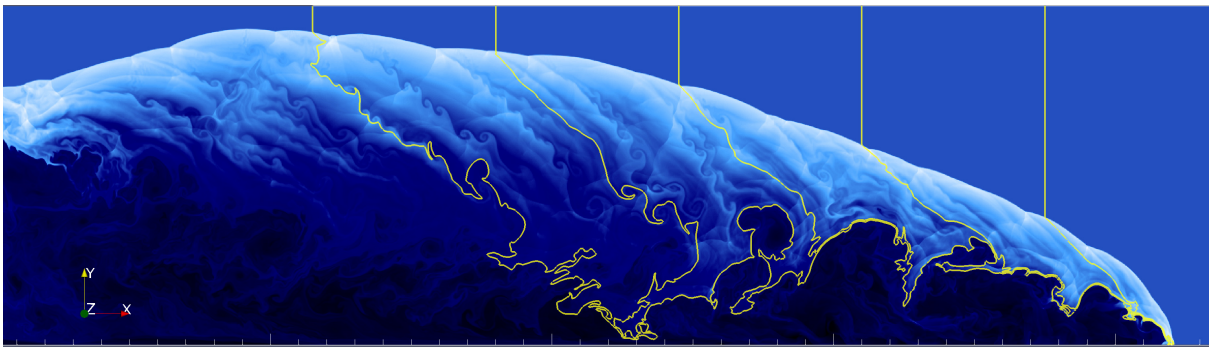

Figure 8. Logarithmic density distribution for model AD2 of Table 1, with $\gamma = 4/3$, $\Gamma = 10$, and $\eta = 10^2$ at $t = 90$. The 5 lines drawn over the density plot represent magnetic field lines, each line starts at the vertical coordinate $y = 12.0$ (top boundary) and horizontal coordinates $x = [11.5, 18.0, 24.5, 31.0$ and $37.5]$.

pressed ambient magnetic field lines depends on η through the propagation velocity of the forward bow shock into the ambient medium (see eqs. 7 to 9), i.e., $\beta_{bs} = \beta_j(1 + L^{-1/2})$, where L measures the ratio between the jet energy density and the ambient rest mass energy density, $L = \mu_j \Gamma_j^2/\eta$, and $\mu_j \sim 1$ is the specific enthalpy of the jet (Bromberg et al. 2011). For the typical large values of $\Gamma_j \sim 10 - 100$ of GRB jets, it turns out that in general $L \ll 1$, even for η varying in a broad range like the one investigated here $\eta = 10^{-4}$ to 10^2, so that β_{bs} and the pile-up effect are nearly insensitive to this parameter.

4.3 Structure function of B and its correlation length

The amplification of B as seen in these models is particularly important because, regardless of the magnetization of the jet itself, as the beam sweeps the ambient gas, the ambient magnetic field lines are dragged, amplified by compression,

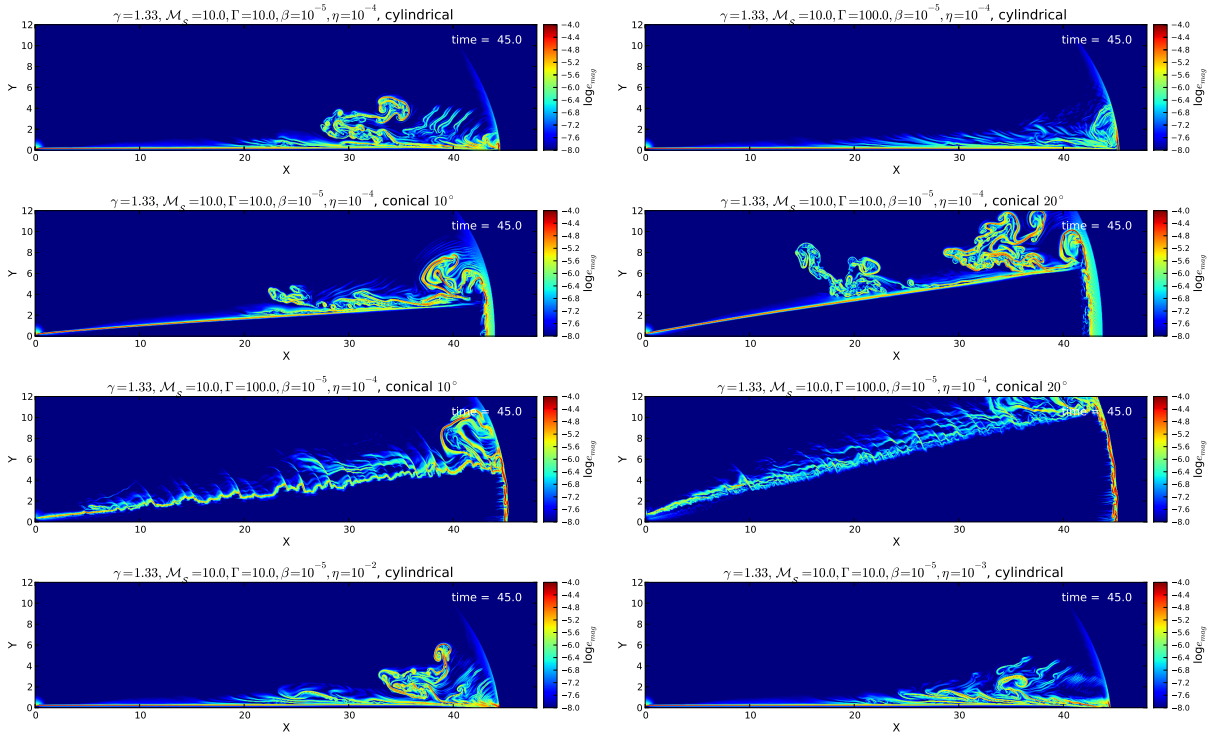

Figure 9. ame description of Fig.3 but for the logarithm of magnetic energy density, for the jet models with $\eta = 10^{-4}$ to $\eta = 10^{-2}$, $\Gamma = 10$ and $\Gamma = 100$ and the opening angle varying between 0° and 20°.

and piled-up into the shock region. Also, as important as the total magnetic field intensity is its correlation length.

In any model of magnetic field amplification, theoretical predictions must also provide arguments for obtaining sustainable large scale magnetic fields.

One way of determining the correlation length of the magnetic field distribution is by means of the second order structure function (SF) (e.g. Kowal et al. 2007; Falceta-Gonçalves et al. 2008), defined as:

$$\mathrm{SF}(l) = \langle |\mathbf{B}(\mathbf{r}+\mathbf{l}) - \mathbf{B}(\mathbf{r})|^2 \rangle, \qquad (16)$$

where $\mathbf{B}(\mathbf{r})$ represents the magnetic field vector at a given position $\mathbf{r}$, and $\mathbf{l}$ the spatial increment for the structure function. The increment l is a vector taken to be parallel to the local orientation of the field line. In this sense the SF measures the statistical changes on the magnetic field along the streamlines. Notice that $\mathrm{SF}_{l\to 0} \to 0$, while as l increases the structure function also increases up to a saturation level. The scale length at which the SF saturates represents the largest scales of the magnetic fluctuations, i.e. the correlation length.

We performed the structure function calculations for the magnetic field lines anchored into the shock head only - this because we focus on determining the correlation length of the maximum amplified magnetic fields. In Fig.11 we present the SFs (S) obtained for the selected adiabatic models. The non-adiabatic models were not plotted to avoid superposition with the depicted curves, as they present very similar profiles to those of the adiabatic counterparts.

For light jets with $\eta = 10^2$, the saturation of the SFs occurs, in all models, at length scales of which represent $l_{\rm sat} \simeq 0.35 - 0.46$ in code units. These values correspond to $\sim 3 - 5$ times the shock thickness λ for the adiabatic and non-adiabatic models, respectively. Heavy jets with $\eta = 10^{-4}$ present larger coherence lengths. For these models the saturation of the SFs occurs at lengthscales in the range of $l_{\rm sat} \simeq 60 - 200$ pixels, depending on the opening angle of the jet, which represents $l_{\rm sat} \simeq 2.3$ in code units. Larger coherence lengths occur for smaller opening angles.

5 DISCUSSION AND CONCLUSIONS

In this work we have explored the possible magnetic field amplification and correlation lengths behind the shock head region of non-magnetized, light and heavy relativistic jets propagating into weakly magnetized environments aiming at comparisons with GRB jet afterglows scenarios in a matter dominated regime. For this we have carried out 2D relativistic MHD (RMHD) simulations considering different values of the jet bulk Lorentz factor (Γ = 2, 10, and 100) and the density ratio between the jet and the environment ($\eta = \rho_{amb}/\rho_j = 10^{-4} - 10^2$). We have focussed on relativistic adiabatic jets (with an adiabatic index $\gamma = 4/3$), but for comparison have also considered systems with $\gamma = 1.1$ in order to mimic the effects of a potential strong thermal radiative cooling in the shocked ambient material at the jet head. All the jets were expanded for approximately the same extension, so that the jet with the highest Lorentz factor was the less evolved one. We have also tested the effects of the jet geometry, considering different opening angles from $\theta = 0°$ (cylindrical jet) to $\theta = 20°$. Our findings are summarized below.

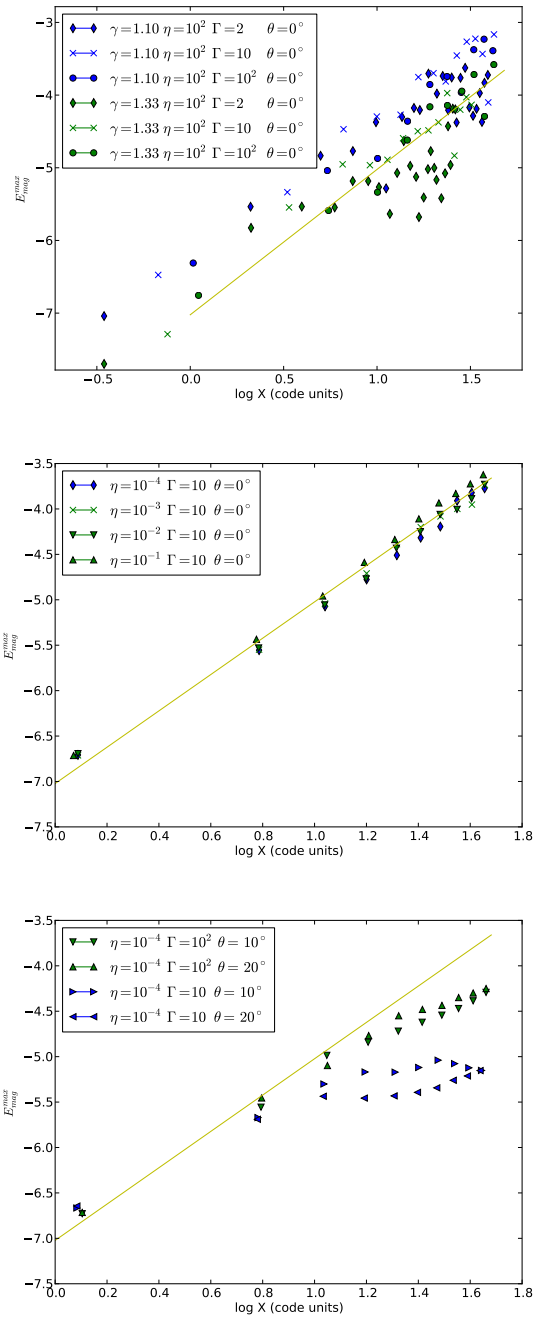

Figure 10. Maximum magnetic energy density (in erg cm^{-3}) as a function of the jet head position; top: cylindrical ($\theta = 0$) light jets, middle: cylindrical ($\theta = 0$) heavy jets, and bottom: wide jets, with different Lorentz factors, and opening angles. The correlation $E^{\rm mag}_{\rm max} \propto B^2_{\rm max} \propto x^2$ is very similar for all collimated jet models. The solid line with a slope of $\zeta = 2$ was drawn for reference.

The magnetic field is amplified by shock compression and accumulates at the contact discontinuity (pile-up effect), with a maximum value that increases with the distance as the jet propagates. The predicted relationship between the magnetic field intensity and the distance as described in Eqs. 7, 8 and 11, was confirmed by the simulations. In particular,

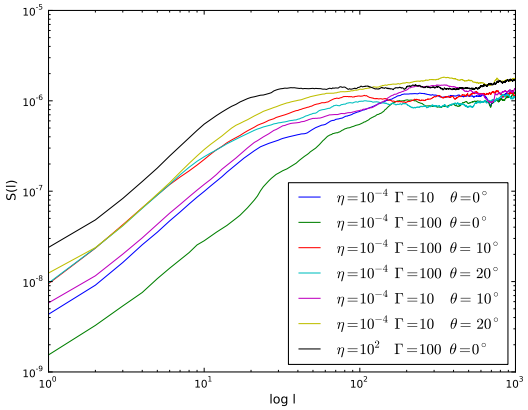

Figure 11. Structure functions (SFs) of magnetic field lines for models varying the parameters η, Γ, and the opening angle. The horizontal axis is shown in number of pixels. Notice that the SFs are calculated along the magnetic field lines and the total pathways are therefore larger than the size of the box.

we have found that the increase in the magnetic field amplification, though initially similar for both collimated and wide jets, saturates earlier for increasing jet opening angles. This effect is smaller as the jet Lorentz factor increases. These results have been found to be nearly insensitive to the density ratio η, but heavier jets present larger magnetic field coherence lengths than lighter ones. Also smaller coherence lengths have been found for larger jet opening angles. In summary, heavy, collimated jets tend to maximize the piling-up and the coherence length of the magnetic field lines.

The results above have been also found to be nearly independent on the adiabatic index (γ), although the maximum intensities of the compressed magnetic fields are a little larger in the non-adiabatic cases, as one should expected from the jump conditions and the larger density amplification behind the shocks in these cases. This general behaviour can be explained by the fact that, after a maximum compression behind the double shock structure at the jet head, the magnetized shocked material is forced to expand sideways, along the cocoon that surrounds the jet. Apparently, all the cases reach similar saturation ratios for the density and magnetic field at the contact discontinuity, regardless of the differences in the jet upstream conditions. Nevertheless, these differences obviously affect the final state of the shocked material that deposits into the cocoon which is clearly distinct in each of the simulated systems as discussed in Section 4.1 (see Figs.3 and 7).

We notice here that in more realistic calculations, with a more consistent treatment of the radiative cooling, the effective value of γ would not be homogeneous over the whole computational domain. The 'non-adiabatic' models above actually represent extreme examples. In more realistic models, with an adiabatic jet beam (with $\gamma = 4/3$) interacting with a radiative cooling cocoon, we would expect the beam structure to be less affected by the shocked cooled gas of the cocoon than in Fig.3 and the propagation velocity of the jet head slightly smaller.

Since we have considered a very broad parametric space,

the results above can be in principle applicable to all classes of relativistic jets, including microquasars, AGNs and GRBs, but below we will discuss the implications for the afterglow emission of GRB jets.

5.1 Implications for GRB afterglows

5.1.1 Magnetic field amplification

Observations of the afterglow phase of GRBs are explained by synchrotron emission of electrons interacting with nearly equipartition magnetic field intensities of $B_{\rm equip} \sim 1$G, at distances of $\sim 10^{15}$cm away of the central source (see review of Piran 2005). As explained in Section 2 the equipartition radius for the magnetic field amplification depends on the shock width λ, which can be roughly estimated from Equation 10 (see also Eq. 11). In this equation, as stressed in Section 2, we need the jet radius at the breakout from the stellar progenitor envelope. This can be estimated from previous analytical and numerical studies of GRB jets (e.g., Zhang, Woosley & MacFadyen 2006; Mizuta & Aloy 2009, Bromberg et al. 2014, Levinson & Begelman 2013, Mizuta & Ioka 2013). For a Poynting flux dominated jet propagating inside the envelope of a Wolf-Rayet progenitor, analytical predictions suggest that $r_j \sim r_L \sim 10^7$ cm, where r_L is the radius of the light cylinder near the source (Levinson & Begelman 2013, Bromberg et al. 2014), while for matter dominated jets r_j can be larger. Numerical simulations indicate $r_j \sim 10^9$ cm (Zhang, Woosley & MacFadyen 2006; Mizuta & Aloy 2009, Mizuta & Ioka 2013). Thus, if we assume r_j at the breakout to be $r_j \sim 10^7 - 10^9$cm, and $\eta = 10^{-4}-10^2$, then we obtain $\lambda \sim 10^3-10^{11}$cm. Despite the simplified geometry, and absence of magnetic field, assumed on the estimation of Eq.10, these values are in rough agreement with the λ/r_j ratio observed in the simulations. In this case, equipartition should occur at $x_{bs} \sim 10^9 - 10^{17}$cm. These values are compatible with the observed afterglow distances ($\sim 10^{15}$cm).

It is worth mentioning that the calculation above considers the magnetic field estimated assuming equipartition between the magnetic and relativistic particles component of the synchrotron emitting plasma. In principle, the equipartition magnetic field at the emitting region may strongly deviate from the actual saturation magnetic field, which is related to the dynamical equilibrium between the jet kinetic pressure and the downstream magnetic field. It is difficult to estimate the later from a physical background since the dynamical evolution of the jet as it propagates through the medium is hardly known *a priori*. For this reason, the numerical simulations may provide a good insight. The saturation on the amplification of the magnetic field can be estimated from the conservation of momentum equation, at the shock reference frame at the jet axis, as:

$$\rho_j \Gamma_j^2 (\beta_j - \beta_{sh})^2 \approx \rho_a \beta_{sh}^2 + \frac{B_s^2}{8\pi\Gamma_s^2} \qquad (17)$$

where $\beta = v/c$, and indices j, a and sh stand for jet, ambient and shock, respectively. For instance, in model AD3, with $\Gamma_j = 100$ and $\rho_a = 100\rho_j = 1.67 \times 10^{-24}$, we obtained $\Gamma_s \sim 2.3$, i.e. $\beta_{sh} \sim 0.9$. Therefore, the saturation in the simulation would occur for $B_s \sim 1.4$G, in agreement with the observations. Naturally, this condition is even more confortable for heavy jets ($\rho_a \ll \rho_j$), for which one obtains a much larger limit $B_{\rm sh} \gg 1$G.

For jets with opening angles, i.e. $\theta_{\rm j} > 0^\circ$, the maximum amplification is reduced. Our results indicate that wide jets present similar behaviour as their cylindrical collimated counterparts at small distances, for which the conclusions made above would be sustained. This is not true though at larger distances. While the well collimated jets result in a quasi indefinitely increase of magnetic pressure (until equipartition is reached), jets with large opening angles saturate at earlier stages. Here the main cause for the saturation os not equipartition but the widening of the shock region width. In conical jets the ratio between the fluxes out and inwards the shocked region becomes smaller with time, resulting in the width growth. Models with $\theta = 20^\circ$ saturate with $B_{\rm max}$ approximately 1 order of magnitude smaller than those with $\theta = 10^\circ$. As the width of the shock region increases, the amplification of the magnetic field is smaller for a lower saturation value in agreement with Eq.7. For instance, for a $\tan\theta \sim 0.1$ and $\Gamma \sim 10^2$ jet, the saturation radius is expected to be at $\simeq 10^3 r_{\rm j} \sim 10^{12}$cm and, as shown above, this length scale would be large enough to amplify the magnetic fields to the observed intensities.

However, despite the apparent sufficient amplification factors obtained from the pile-up process, the large magnetization of the observed afterglow emission cannot be fully explained yet. In the current GRB paradigm, adopted in this work, the afterglow emission is assumed to be radiated from the freshly injected plasma at vicinity of the shock. It should be further noticed that the freshly injected plasma, just downstream of the shock, is weakly magnetized[4]. The main effect of pile-up only occurs as the matter flows further downstream whereas the frozen field slowly grows. Though the field strength could be large it peaks at the contact discontinuity region, which is at a distance $\sim \lambda$ of the freshly injected shocked plasma, where particles are supposed to accelerate. Therefore the pile-up effect, even if it is strong enough, may not directly affect the afterglow emission in such a scenario, and would not provide "the" solution to the magnetization problem in GRBs.

5.1.2 Correlation lengths

Also, by means of second order structure functions (SFs), we obtained the correlation lengths of the amplified magnetic fields at the jet head. We find $l_{\rm corr} \sim 3-5\lambda \sim 10^8 - 10^{12}$cm for light jets, and $\sim 10^9 - 10^{14}$cm for the heavy jet models. There is no obvious trend between the correlation length and the jet opening angle. For the Weibel instability the correlation lengths obtained are of the order of the plasma skin depth, i.e. $\delta = (c/\omega_p) \sim 10^6$cm, while observations point towards much larger correlation lengths, of 10^{16}cm (e.g. Waxman 2006).

Still the values obtained in this work are 2 orders of magnitude smaller than those obtained from observations. Since our models revealed that the correlation length depends on the jet-to-ambient gas density ratio, heavier jets, compared to those simulated here, would result in larger

[4] as given by the standard Rankine-Hugoniot conditions.

$l_{\rm corr}$, closer to observations. Another possible solution to this problem is that, due to the strong downstream turbulence as seen in part of our models, magnetic reconnection could be induced resulting in more uniform fields. Considering that the equipartition occurs at short timescales (specially for jets), any magnetic energy loss due to reconnection would be shortly replenished by further piled-up field lines. It is possible then that the field lines would have larger observed correlation lengths once the systems reaches the afterglow phase.

In any case, the fact that our present study of unmagnetized jets impinging into a magnetized ISM results magnetic correlation lengths in the shock front 2 orders of magnitude smaller than the expected for GRBs points to the necessity of exploring the magnetic field amplification and pile-up in magnetized relativistic jets. The recent polarization observations by Wiersema et al. (2014) indicate that this may be the correct way to solve this question.

5.2 Final Remarks

Two further important remarks are in order. First, we have assumed a two-dimensional (2D) jet geometry. A more realistic 3D geometry can reduce the pile-up efficiency since this geometry allows another degree of freedom for the magnetic field lines (and gas) to leave the shock region. However, since in this case the degree of freedom of field lines is still smaller than that of the gas, the pile-up must still occur, though not as efficient as in the two-dimensional well-collimated jet case. We stress that the main goal of this work was not to reproduce the actual emission properties of the afterglow, but to verify if the magnetic field could be amplified in the jet-envelope shock context. In order to determine exactly the emission properties, on top of the amplification process, three-dimensional simulations are mandatory.

A third dimension will naturally introduce another degree of freedom for the downstream flow, which implies an extra dimension to which magnetic field lines may be carried away from the shock region thus decreasing the pile-up effect. We may therefore expect that in a 3D jet model the amplification of the magnetic field intensity will slow down, but the final picture of the pile-up in this case is still unknown. Another possible effect that was not taken into account in our study regards the fact that, at the time that the jet breaks out from the stellar surface into the ambient medium, the GRB central engine has probably turned off already. This implies that the continuous injection should stop, giving place to a propagating jet parcel with a forward bow shock at the head slowly detaching from the reverse shock. This effect will also weaken the piling-up of the magnetic field in the bow shock. Both effects will be investigated in depth in a forthcoming work.

However, even in the case of efficient pile-up we must be careful in attributing to this mechanism the solution for the magnetization problem in the afterglow emission. The magnetic energy in our models has been found to be concentrated at the contact discontinuity while the emitting particles are expected to be located the the downstream side of the shock surface. A large distance between these two different regions result in an effective low magnetization where the emitting particles actually are. This issue must be pursued in forthcoming works.

Finally, as stressed before, the afterglow emission is generally believed to be due to relativistic particles accelerated by a first-order Fermi process occurring mostly at the shock region, at the jet head. Examining Fig.7, we note that other regions in the beam and the cocoon than the shock head itself have also reached a magnetized turbulent structure with high intensity magnetic fields. These magnetic fields, in part also amplified by the instabilities developed in the cocoon and by turbulent shear, can equally help to accelerate particles to relativistic velocities. In these regions, first-order Fermi acceleration by magnetic reconnection, as first proposed by (de Gouveia dal Pino & Lazarian 2005), can be also very efficient, as well as second order Fermi to preaccelerate the particles, as indicated by recent numerical MHD studies of particle acceleration in different domains of magnetic reconnection (Kowal et al. 2012) (see also de Gouveia Dal Pino & Kowal 2013, for a review). This issue will be further explored by means of "in situ" particle acceleration simulations in relativistic jets as in de Gouveia Dal Pino & Kowal (2013) where preliminary tests have been presented (see also applications to GRBs in Giannios (2010); Cerutti et al. (2013)).

ACKNOWLEDGMENTS

G.R.S. thanks CNPQ for financial support. D.F.G. thanks the European Research Council (ADG-2011 ECOGAL) and the Brazilian agencies CNPq (No. 300382/2008-1), CAPES (3400-13-1) and FAPESP (No. 2011/12909-8) for financial support. G.K. thanks FAPESP (No. 2009/50053-8, 2011/51275-4, 2013/04073-2, 2013/18815-0) for financial support. E.M.G.D.P. thanks FAPESP (No. 2006/50654-3) and CNPq (306598/2009-4) for financial support. The authors also acknowledge very fruitful discussions with T. Piran, J. Stone and G. Lugones. This work has made use of the computing facilities of the Laboratory of Astroinformatics (IAG/USP, NAT/Unicsul), purchased by FAPESP (grant 2009/54006-4), and of the Hydra cluster at EACH-USP.

REFERENCES

Aloy, M.A., Ibáñez, J.M., Martí, J.M., Gómez, J.L., Müller, E. 1999, ApJL, 523, L125
Appl, S., & Camenzind, M. 1988, A&A, 206, 258
Begelman, M. C., & Cioffi, D. F. 1989, ApJL, 345, L21
Beniamini, P., & Piran, T. 2014, ApJ, 769, 69
Birkinshaw, M. 1996, Ap&SS, 242, 17
Blandford, R. D. & McKee, C. F. 1976, Phys. Fluids, 19, 1130
Blondin, J. M., Fryxell, B. A., & Konigl, A. 1990, ApJ, 360, 370
Bloom, J. S.; Frail, D. A.; Kulkarni, S. R. 2003 ApJ, 594, 674
Bodo, G., Mamatsashvili, G., Rossi, P., & Mignone, A. 2013, MNRAS, 434, 3030
Bogovalov, S. V. 1996, MNRAS, 280, 39
Bromberg, O., Granot,J., Lyubarsky, Y., & Piran, T. 2014, MNRAS, 443, 1532
Bromberg, O., Nakar, E., Piran, T., & Sari, R. 2011, ApJ, 740, 100

Cerqueira, A. H., de Gouveia Dal Pino, E. M., & Herant, M. 1997, ApJL, 489, L185
Cerutti, B., Werner, G. R., Uzdensky, D. A., & Begelman, M. C. 2013, ApJ, 770, 147
Chernin, L., Masson, C., de Gouveia Dal Pino, E. M., & Benz, W. 1994, ApJ, 426, 204
Chiueh, T., Li, Z.-Y., & Begelman, M. C. 1991, ApJ, 377, 462
De Colle, F., Ramirez-Ruiz, E., Granot, J., & López-Cámara, D. 2012, ApJ, 751, 57
de Gouveia Dal Pino, E. M., & Benz, W. 1993, ApJ, 410, 686
de Gouveia Dal Pino, E. M., & Benz, W. 1994, ApJ, 435, 261
de Gouveia Dal Pino, E. M., & Kowal, G. 2013, arXiv:1302.4374
de Gouveia Dal Pino, E. M., & Lazarian, A. 2005, A&A, 441, 845
de Gouveia Dal Pino, E. M. 2005, Advances in Space Research, 35, 908
Dedner, A., Kemm, F., Kröner, D., et al. 2002, Journal of Computational Physics, 175, 645
Eichler, D., & Cheng, A. F. 1989, ApJ, 336, 360
Falceta-Gonçalves, D., & Abraham, Z. 2012, MNRAS, 423, 1562
Falceta-Gonçalves, D., Lazarian, A., & Kowal, G. 2008, ApJ, 679, 537
Falceta-Gonçalves, D., de Gouveia Dal Pino, E. M., Gallagher, J. S., & Lazarian, A., 2010, ApJL, 708, L57
Falceta-Gonçalves, D., Caproni, A., Abraham, Z., Teixeira, D. M., & de Gouveia Dal Pino, E. M., 2010, ApJL, 713, L74
Falceta-Gonçalves, D., Lazarian, A., & Houde, M., 2010, ApJ, 713, 1376
Falceta-Gonçalves, D. & Monteiro, H. 2014, MNRAS, 438, 2853
Folini, D., & Walder, R. 2000, Ap&SS, 274, 189
Folini, D., & Walder, R. 2006, A&A, 459, 1
Frederiksen, J. T., Hededal, C. B., Haugbølle, T., & Nordlund, Å. 2004, ApJL, 608, L13
Frail, D. A.; Kulkarni, S. R.; Sari, R.; Djorgovski, S. G.; Bloom, J. S.; Galama, T. J.; Reichart, D. E.; Berger, E.; et al. 2001, ApJ, 562, 55
Galama, T. J., Briggs, M. S., Wijers, R. A. M. J., et al. 1999, Nature, 398, 394
Gallant, Y. A., Hoshino, M., Langdon, A. B., Arons, J., & Max, C. E. 1992, ApJ, 391, 73
Giannios, D., & Spruit, H. C. 2006, A&A, 450, 887
Giannios, D. 2010, MNRAS, 408, L46
Godunov, S. K. 1959, "A Difference Scheme for Numerical Solution of Discontinuous Solution of Hydrodynamic Equations", Math. Sbornik, 47, 271306, translated US Joint Publ. Res. Service, JPRS 7226, 1969
Granot, J., Konigl, A. 2001, ApJ, 560, 145
Granot, J., Komissarov, S. S., & Spitkovsky, A. 2011, MNRAS, 411, 1323
Granot, J. 2012, MNRAS, 421, 2467
Gruzinov, A. 2001, ApJL, 563, L15
He, Z., Li, X., Fu, D., & Ma, Y. 2011, Science in China G: Physics and Astronomy, 54, 511
Hededal, C. B., Haugbølle, T., Frederiksen, J. T., & Nordlund, Å. 2004, ApJL, 617, L107
Heyvaerts, J., & Norman, C. 1989, ApJ, 347, 1055
de Hoffmann, F. & Teller, E., 1950, Physical Review, 80, 692
Hughes, P. A., Miller, M. A., & Duncan, G. C. 2002, ApJ, 572, 713
Kazimura, Y., Sakai, J. I., Neubert, T., & Bulanov, S. V. 1998, ApJL, 498, L183
Kennel, C. F., & Coroniti, F. V. 1984, ApJ, 283, 694
Keppens, R., Meliani, Z., van der Holst, B., & Casse, F. 2008, A&A, 486, 663
Komissarov, S. S. 1999, MNRAS, 308, 1069
Kowal, G. & Lazarian, A., 2010, ApJ, 720, 742
Kowal, G., Lazarian, A., & Beresnyak, A. 2007, ApJ, 658, 423
Kowal, G., de Gouveia Dal Pino, E. M., & Lazarian, A., 2011, ApJ, 735, 102
Kowal, G., Falceta-Gonçalves, D. A., & Lazarian, A. 2011, NJPh, 13, 3001
Kowal, G., de Gouveia Dal Pino, E. M., & Lazarian, A., 2012, Physical Review Letters, 108, 241102
Lazzati, D., & Begelman, M. C. 2005, ApJ, 629, 903
Lazzati, D., Morsony, B. J., & Begelman, M. C. 2009, ApJL, 700, L47
Leismann, T., Antón, L., Aloy, M. A., et al. 2005, A&A, 436, 503
Levinson, A., & Begelman, M. C. 2013, ApJ, 764, 148
Li, Z., & Zhao, X.-H. 2011, Journal of Cosmology and Astroparticle Physics, 5, 8
López-Cámara, D.; Morsony, Brian J.; Begelman, Mitchell C.; Lazzati, D. 2013, ApJ, 767, 19
Lugones, G., Ghezzi, C. R., de Gouveia Dal Pino, E. M., & Horvath, J. E. 2002, ApJL, 581, L101
Lyubarsky, Y. 2009, ApJ, 698, 1570
Lyubarsky, Y. 2010, ApJL,725, L234
Lyutikov, M., & Blandford, R. 2003, arXiv:astro-ph/0312347
MacFadyen, A. I., & Woosley, S. E. 1999, ApJ, 524, 262
MacFadyen, A. I., Woosley, S. E., & Heger, A. 2001, ApJ, 550, 410
Tchekhovskoy, A.,Narayan, R., & McKinney, J. C. 2010, NewA, 15, 749
McKinney, J. C., & Uzdensky, D. A. 2012, MNRAS, 419, 573
Mallick, R. 2011, Phys. Rev. C, 84, 065805
Marti, J. M. A., Mueller, E., Font, J. A., Ibanez, J. M. A., & Marquina, A. 1997, ApJ, 479, 151
Medvedev, M. V., & Loeb, A. 1999, ApJ, 526, 697
Meszaros, P., & Rees, M. J. 1997, ApJL, 482, L29
Mignone, A., & Bodo, G. 2006, MNRAS, 368, 1040
Mignone, A., & McKinney, J. C. 2007, MNRAS, 378, 1118
Mignone, A., Plewa, T., & Bodo, G. 2005, ApJs, 160, 199
Mizuta, A., & Aloy, M. A. 2009, ApJ, 699, 1261
Mizuta, A., & Ioka, K. 2013, ApJ, 777, 162
Morsony, B.J., Lazzati, D., & Begelman, M. C. 2007, ApJ, 665, 569
Nava, L., Sironi, L., Ghisellini, G., Celotti, A., & Ghirlanda, G. 2013, MNRAS, 433, 2107
Nishikawa, K.-I., Hardee, P., Richardson, G., et al. 2003, ApJ, 595, 555
Nishikawa, K. -., Hardee, P., Richardson, G., et al. 2004, arXiv:astro-ph/0409702

Noble, S. C., Gammie, C. F., McKinney, J. C., & Del Zanna, L. 2006, ApJ, 641, 626
Paczyński, B. 1998, Gamma-Ray Bursts, 4th Hunstville Symposium, 428, 783
Paczyński, B. 1986, ApJL, 308, L43
Perucho, M. 2012, International Journal of Modern Physics Conference Series, 8, 241
Piran, T. 1999, Phys.Rept., 314, 575
Piran, T. 2005, Magnetic Fields in the Universe: From Laboratory and Stars to Primordial Structures., 784, 164
Poidevin, F., Falceta-Gonçalves, D., Kowal, G., de Gouveia Dal Pino, E., Magalhaes, A. M. 2013, ApJ, 777, 112
Raga, A., & Cabrit, S. 1993, A&A, 278, 267
Rees, M. J., & Meszaros, P. 1992, MNRAS, 258, 41P
Rhoads, J.E. 1999, ApJ, 525, 737
Ruiz, L. O., Falceta-Gonçalves, D., Lanfranchi, G. A. & Caproni, A. 2013, MNRAS, 429, 1437
Ruuth, S. J. 2006, Mathematics of Computation, 75, 183
Santana R., Barniol Duran R. & Kumar P. 2014, ApJ, 785, 29
Santos-Lima, R., Lazarian, A., de Gouveia Dal Pino, E. M., & Cho, J. 2010, ApJ, 714, 442
Santos-Lima, R., de Gouveia Dal Pino, E. M., & Lazarian, A. 2012, ApJ, 747, 21
Santos-Lima, R., de Gouveia Dal Pino, E. M., & Lazarian, A. 2013, MNRAS, 429, 3371
Sari, R., Narayan, R., & Piran, T. 1996, ApJ, 473, 204
Sari, R.; Piran, T. & Halpern, J.P. 1999, ApJL, 519, 17
Shemi, A., & Piran, T. 1990, ApJL, 365, L55
Stone, J. M., & Norman, M. L. 1993, ApJ, 413, 198
Summerlin, E. J., & Baring, M. G. 2012, ApJ, 745, 63
Suresh, A., & Huynh, H. T. 1997, Journal of Computational Physics, 136, 83
Thompson, C. 1994, MNRAS, 270, 480
Tchekhovskoy, A., McKinney, J. C., & Narayan, R. 2008, MNRAS, 388, 551
Tchekhovskoy, A.,McKinney, J. C., & Narayan, R. 2009, ApJ, 699, 1789
Usov, V. V. 1992, Nature, 357, 472
van der Holst, B., Keppens, R., & Meliani, Z. 2008, Computer Physics Communications, 179, 617
Viegas, S. M., & de Gouveia dal Pino, E. M. 1992, ApJ, 384, 467
Vishniac, E. T. 1994, ApJ, 428, 186
Waxman, E. 1997, ApJL, 485, L5
Waxman, E. 2006, Plasma Physics and Controlled Fusion, 48, 137
Wiersema,K. et al. 2014, Nature, 13237
Woosley, S. E. 1993, ApJ, 405, 273
Yost, S. A., Harrison, F. A., Sari, R., & Frail, D. A. 2003, ApJ, 597, 459
Zeh, A.; Klose, S.; Kann, D. A. 2006, ApJ, 637, 889
Zhang, W., Woosley, S. E., & MacFadyen, A. I. 2003, ApJ, 586, 356
Zhang, B., & Yan, H. 2011, ApJ, 726, 90
Zhang, B. 2011, Comptes Rendus Physique, 12, 206